Lithosphere Removal in the Sierra Nevada de Santa Marta, Colombia

D. E. Quiroga[1], C. A. Currie[1] and J. Pearse[2]

[1]Department of Physics, University of Alberta, Edmonton, AB T6G 2E1, Canada
[2]Department of Geociences, Universidad de los Andes, Bogotá, Colombia

Key Points:

- Mantle lithosphere and crustal root are gravitationally removed as local drips, generating a thinned crust within 25 Ma
- Removal event can explain the observed high topography and positive Bouguer gravity anomaly for the Sierra Nevada de Santa Marta, Colombia
- Non-isostatic forces have a significant role in the support of high topography during removal

Corresponding author: David Quiroga, dquiroga@ualberta.ca

Abstract

The Sierra Nevada de Santa Marta (SNSM) in northwestern Colombia is one of the world's highest coastal mountains, with an elevation above 5.7 km. Gravity measurements show that the SNSM has a high Bouguer anomaly (>+130 mGal), indicating that the mountain lacks a crustal root. In this work, we test the hypothesis that these observations can be explained by gravitational removal of the dense lower lithosphere. We use 2D numerical models to examine the dynamics of lithosphere removal and its effect on surface elevation, gravity and heat flow. The models consist of continental lithosphere that includes a pre-thickened crustal region, representing the SNSM. In our preferred model, the dense mantle lithosphere instability and crustal root are gravitationally unstable and undergo removal as local drips within ∼10 Ma from the onset of foundering. This creates an area of thinned crust (∼38 km) underlain by a buoyant sublithospheric mantle where melting and low seismic velocities are predicted. Subsequent non-isostatic forces maintain a topography of 3.3 km with a Bouguer gravity anomaly of +103 mGal. Parameter tests show that a strong lower-crustal rheology provides greater support for the high topography and that a weak mantle lithosphere rheology produces faster removal. The models demonstrate that local lithosphere dynamics can explain the first-order observations in the SNSM. We propose that lithosphere removal could have occurred at 40-50 Ma, possibly inducing anomalous short-lived Eocene magmatism, or more recently (∼2 Ma), explaining the localized low seismic velocity zone below the SNSM.

Plain Language Summary

Most high mountain regions are formed during continental deformation near tectonic plate boundaries, creating an area of thick low-density crust. The Sierra Nevada de Santa Marta (SNSM) is an unusual mountain in northwestern Colombia. It is isolated from the main Andes Mountain belt, but it has an elevation above 5.7 km and geophysical measurements indicate that the crust is unexpectedly thin. Here, we test the idea that the SNSM once had a thick crust, but the lower part of this layer was anomalously dense and sank into the deep mantle. We use 2D computer simulations to investigate this phenomenon and its effect on the Earth's surface. The models start with a ∼125 km wide area with a thicker crust and a deflection in the underlying rigid mantle lithosphere. Because the mantle lithosphere is cooler and denser than the mantle below, it sinks as a drip. This process induces an increase in the density of the lower crust such that it also sinks as a drip. The models show that the removal leaves a high elevation region with a locally thin crust that is underlain by a low seismic wave velocity zone and melting, consistent with SNSM observations.

1 Introduction

The Sierra Nevada de Santa Marta (SNSM) in northern Colombia has a maximum height of ∼5.7 km (Figure 1*a*). This triangular shaped mountain region is isolated from the Andes Cordillera, and yet it has the highest peak in Colombia. Early geophysical observations show that this region has a positive Bouguer gravity anomaly of more than +130 mGal (Case & Macdonald, 1973) (Figure 1). This is unexpected because high mountains are typically supported by thick crustal roots, producing a negative gravity anomaly. Consequently, it is argued that the high elevations in the SNSM massif are not supported by an Airy-type crustal root (e.g., Ceron-Abril, 2008; Montes et al., 2005; Villagómez et al., 2011) and instead, that there is a thin crust to explain the positive gravity anomaly (Case & Macdonald, 1973). Indeed, crustal thickness estimations based on wide-angle seismic refraction, seismic receiver functions, and surface geology, suggest a locally thin crust (i.e., 30-35 km) for the SNSM (Sanchez-Rojas & Palma, 2014). This raises the questions of how the massif is mechanically supported and why there is no crustal root.

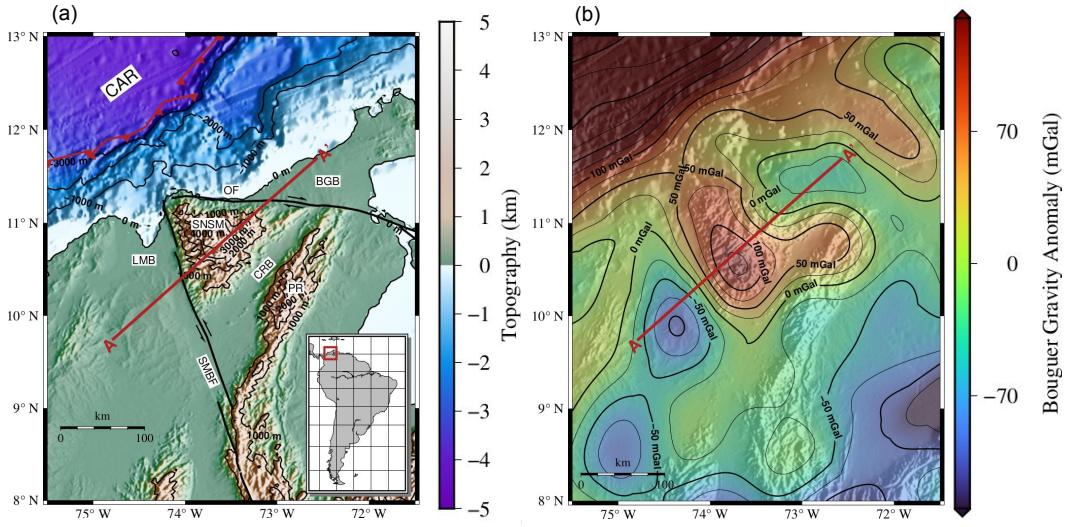

Figure 1. (a) Topographic map of the study region in northern Colombia. BGB: Baja Guajira Basin, OF: Oca Fault, SNSM: Sierra Nevada de Santa Marta, LMB: Lower Magdalena Basin, CRB: Cesar-Rancheria Basin, PR: Perijá Range, SMBF: Santa Marta-Bucaramanga Fault. The barbed line is the plate margin where the Caribbean plate (CAR) converges with South America. (b) Bouguer gravity anomaly map from the EIGEN-GL04C Global gravity field model (Förste et al., 2008). Profiles of topography and gravity anomaly from A to A′ are used to compare the models with observations.

One possibility is that the underthrusting of the buoyant Caribbean plateau and oceanic seamounts could provide support for the SNSM topography (e.g., Case & Macdonald, 1973; Montes et al., 2005). In addition, Montes et al. (2005) propose that the Caribbean slab could have caused an upward bulge of the continental Moho, creating a thin SNSM crust and positive gravity anomaly. However, if the SNSM is directly underlain by the Caribbean slab, a locally low surface heat flow would be expected because of conductive cooling by the slab. However, the surface heat flow for the SNSM is 60 to 80 mW·m^{-2} (Quintero et al., 2019), indicating a hot lithosphere. Studies by Quintero et al. (2019) and Vargas et al. (2009) using Curie point depth estimations and direct borehole temperature measurements, respectively, also suggest that the lithosphere is relatively hot.

Another possibility is that the SNSM topography is laterally supported by a rigid and strong continental lithosphere, based on elastic thickness values of more than 26 km (Arnaiz-Rodríguez & Audemard, 2014). Tassara et al. (2007) finds elastic thickness values of 30 to 40 km for northern Colombia. While the presence of a rigid lithosphere could provide mechanical support for the high topography, it does not explain the high magnitude positive Bouguer gravity anomaly, meaning that there must be an additional factor that creates an excess of mass.

Another consideration is the timing of development of the high SNSM elevations). Villagómez et al. (2011) used fission track thermochronology to determine the timing of rock exhumation. They find that between the Late Eocene and Early Oligocene (40-30 Ma) there was exhumation at a rate <0.5 mm·yr^{-1}. The last period of exhumation occurred between the Late Oligocene and Miocene (30-16 Ma), where high exhumation rates (>0.5 mm·yr^{-1}) are attributed to underthrusting of the Caribbean plate below northern South America produced by increased convergence rates between the North and South

American plates. Additionally, Villagómez et al. (2011) find no evidence of significant exhumation in the last 16 Ma, which is inconsistent with the high topography and high annual rainfall (1000-2000 mm·yr^{-1}; Peraza (2014)) in this region, and therefore they argue that this reflects uplift in the last 1-2 Ma. From their work, the exhumation between 40-30 Ma and the recent uplift phase (∼2 Ma) are not related to regional tectonics and the driving forces remain unclear.

Here, we explore the idea that the SNSM observations can be explained by local gravitational lithosphere thinning. Previous work has shown that gravitational foundering of the deep lithosphere as a local drip can simultaneously produce lithosphere and/or crustal thinning, surface uplift, and symmetric high topography (e.g., Göğüş & Pysklywec, 2008; H. Wang & Currie, 2017). This mechanism has been proposed to explain unusual surface expressions in various mountain ranges, such as the Sierra Nevada, California, the Puna Plateau of South America, the Wallowa Mountains in northeast Oregon, and the central Anatolian plateau (e.g., Saleeby et al., 2012; DeCelles et al., 2015; Hales et al., 2005; Göğüş et al., 2017). Removal of the lower lithosphere can be produced by the growth of perturbations in the cold, dense mantle lithosphere (Houseman et al., 1981) or by gravitational instability of localized magmatic/metamorphic eclogite (Jull & Kelemen, 2001; H. Wang et al., 2015). As discussed below, the SNSM region has experienced significant shortening, and therefore crustal thickening could have fostered metamorphic eclogitization in the deep crust, simultaneously producing a mantle lithosphere instability. Alternatively, previous stages of arc magmatism in the SNSM region (e.g., Cardona et al., 2010; Duque-Trujillo et al., 2019; Ramírez et al., 2020) could have resulted in the formation of dense residues (also called arclogites) after partial melting or fractionation in the lower crust (Ducea, Chapman, Bowman, & Triantafyllou, 2021). The removal of the dense lower lithosphere would explain the absence of a thick crustal root in the SNSM.

In this study we use 2D numerical models to investigate if the observations of high surface topography, positive Bouguer gravity anomaly and high surface heat flow can be explained by lithosphere removal. Our models explore the effect of different lithosphere rheologies on removal dynamics and the surface expressions. We also examine the effect of denser upper crustal rocks (e.g., Sanchez-Rojas & Palma, 2014) and their influence in the gravity anomaly. We calculate the non-isostatic topography in the models and show that non-isostatic forces may provide significant support for the load of the massif. Additionally, we use the models to predict melting patterns and seismic wave velocities in the upper mantle, as other observations that can be used to identify lithosphere removal.

2 Tectonic/Geologic Background

The SNSM is part of a larger crustal fragment known as the Maracaibo block and is located at its northwestern corner, approximately 100 km southeast of the tectonic margin between the Caribbean and South American plates (Figure 1*a*). At present, the Caribbean plate is obliquely converging with South America at a rate of 10-20 mm·yr^{-1} toward the southeast (e.g., Freymueller et al., 1993). Regional seismological studies show that the Caribbean plate subducts (or underthrusts) the South American plate at a shallow angle (<30°) and the slab is at a depth of 80 to 120 km below the SNSM (e.g., Cornthwaite et al., 2021; Londoño et al., 2020; Taboada et al., 2000; Van Der Hilst & Mann, 1994; Vargas, 2020).

The triangular SNSM massif is bounded by major faults and basins on its three sides (Figure 1*a*). At the north, the SNSM is limited by the right lateral Oca fault and the Baja Guajira basin. At the southwest, it is bounded by the left-lateral Santa Marta-Bucaramanga fault and the Lower Magdalena basin. At the southeast, it is bounded by the Cesar-Rancheria basin and the Perijá range. The Santa Marta-Bucaramanga and Oca faults exceed 200 km in length and have experienced significant lateral displacements since

the Paleocene of 100 km and 65 km, respectively (e.g., Case & Macdonald, 1973; Tschanz et al., 1974).

The SNSM is commonly divided into three geo-tectonic provinces (Tschanz et al., 1974): the Sierra Nevada, Sevilla, and Santa Marta provinces. According to Ramírez et al. (2020) the oldest rocks in the SNSM are in the Sevilla province (The Buriticá and Los Muchachitos gneisses) and Sierra Nevada province (Los Mangos granulite and Dibulla gneiss). These form the Precambrian metamorphic basement (e.g., Sanchez & Mann, 2015). In the Sierra Nevada province, the basement is overlain by Devonian-Carboniferous and late Triassic-Early Jurassic sedimentary rocks (e.g., Cuchilla de Carbonal and Los Indios formation, respectively). These rocks are mostly covered by outcropping Jurassic igneous bodies (Tschanz et al., 1974), which have intermediate to felsic compositions and mafic intrusions (Ramírez et al., 2020). (Quandt et al., 2018) show that these are continental arc plutons associated with a Jurassic magmatic arc. In the Sevilla Province the basement is mostly overlain by Paleozoic metamorphic rocks (e.g., El Encanto orthogneiss, the Sevilla Metamorphic complex). The Santa Marta province is constituted by Cretaceous metamorphic rocks (Santa Marta metamorphic belt) which are intruded by Paleogene arc-type igneous rocks (e.g., Santa Marta Batholith). These rocks show the evolution of northwest South America after the Late Cretaceous. This region was influenced by the collision of the Caribbean large igneous province, starting 75 Ma ago (Spikings et al., 2015). This diachronous collision progressed towards the north during the westward displacement of the South American plate relative to the Caribbean plate (e.g., Bayona et al., 2011; Pindell et al., 2005). The collision was followed by the onset of the shallow subduction of the Caribbean plate below South America in the early Paleocene (Villagómez et al., 2011), which produced magmatism in the NW corner of the SNSM, forming the Santa Marta batholith and other arc-type plutons (Cardona et al., 2010).

3 Methods

3.1 Governing Equations and Modeling Approach

We use 2D numerical models to study the dynamics of lithosphere removal for the SNSM. The models use the ASPECT code version 2.2.0 (Bangerth, Dannberg, Gassmoeller, Heister, & Others, 2020; Heister et al., 2017). The code solves the governing equations of incompressible mass conservation, the momentum conservation, and the heat conservation, using the Boussinesq approximation formulation and assuming plane strain (Kronbichler et al., 2012). We model the thermal-mechanical evolution of the lithosphere and upper mantle, where the thermal and mechanical fields are coupled using temperature-dependent material properties.

We compare the model results to three key surface observables: surface topography, surface heat flow and Bouguer gravity anomaly. The topography is determined by using a stress-free upper boundary that allows dynamic surface deformation throughout the model evolution (Rose et al., 2017). The surface heat flow is calculated by multiplying the vertical temperature gradient at the surface by the thermal conductivity.

The Bouguer gravity anomaly calculation at each timestep, for each horizontal position along the profile, is based on the density differences (anomalies) with respect to the reference (non-perturbed) density structure in Figure 2b. The contribution to the total gravity anomaly of the density difference in each element in the domain is approximated as the anomaly of a finite slab (Telford et al., 1990) (futher details in Quiroga, 2022).

3.2 Initial Setup and Material Properties

The 2D model domain (Figure 2) has a width of 1320 km and height of 660 km representing the continental lithosphere and the upper mantle in the SNSM region. Our model does not include the subducting Caribbean plate because the goal is to model a lithospheric drip and its isolated contribution to surface observables. The mesh has square elements with lengths and widths of 2.58 km in the upper 200 km and 10 km below. The upper region has a finer mesh to properly resolve lithospheric deformation. The side boundary conditions are free slip, the bottom boundary condition is no slip, assuming that the upper mantle is coupled to the high-viscosity lower mantle, and the top boundary has a free surface.

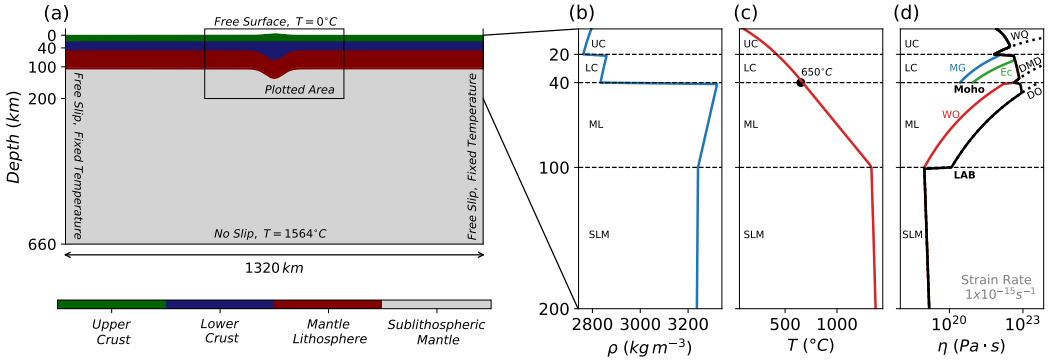

Figure 2. (a) Initial model setup. Only the enclosed region is shown in the following figures. (b) Non-perturbed density structure. (c) Initial temperature conditions. The continental geotherm is stretched in the thickened region keeping the Moho temperature constant. (d) Reference viscosity structure at a constant strain rate of 10^{-15} s^{-1} (black). Black dotted lines show the reference viscous rheologies above plastic yielding including: Wet Quartzite (WQ), Dry Maryland Diabase (DMD), and Dry Olivine (DO). Coloured lines show other viscous rheologies tested including: Eclogite (Ec) with $f = 0.1$, Mafic Granulite (MG) and Wet Olivine (WO). See Table 1 for references.

The continental crust is 40 km thick, with a 20 km upper crust and 20 km lower crust. This is underlain by a 60 km mantle lithosphere. An area of initially thick lithosphere is placed in the middle of the model (Figure 2*a*) to represent the SNSM, assuming the mountain region experienced an earlier episode of shortening. Ramírez et al. (2020) report a continental crust of about 64 ∼km during the Jurassic arc, and subsequent collision of the Caribbean plateau in the Late Cretaceous-Erly Paleocene is inferred to have produced further thickening (Villagómez et al., 2011). In the model, the thickened region consists of an initial surface topography and crustal root, where the deflections have gaussian shapes with half-widths of 62.5 km, resembling the width of the SNSM. At its maximum, the total crustal thickness in this region is about 35 km thicker than the undisturbed crust. The amplitude of the initial topography is set to be in isostatic balance under the assumption that equilibrium occurred right after or during shortening. The crustal thickening results in a perturbation in the lithosphere-asthenosphere boundary (LAB). In this work, we do not model shortening but rather we look at the dynamic response after crustal thickening. The zero topography corresponds to the non-perturbed surface (upper boundary) at the sides of the thickened region in the modeling setup (Figure 2*a*).

All materials have temperature-dependent densities and viscous-plastic rheologies using the material properties given in Table 1. The reference model (model A) is based

Table 1. Model parameters for the reference model (model A). The reference model does not include eclogitization. The paremeters for eclogite are used in all the other models in this work.

Parameter	Upper Crust	Lower Crust		Eclogite	Mantle Lithosphere	Sublithospheric Mantle
Density[a]						
$\rho_0\,(kg\,m^{-3})$	2800	2900		3550	3400	3400
$\alpha\,(K^{-1})$	3×10^{5}	3×10^{5}		3×10^{5}	3×10^{5}	3×10^{5}
Plastic rheology[b]						
ϕ	$15°-2°$	$15°-2°$		$15°-2°$	$15°-2°$	$15°-2°$
$C\,(MPa)$	$20-2$	$20-2$		$20-2$	$20-2$	$20-2$
Viscous rheology[c]	*Wet Quartzite*	*Dry Diabase*	*Mafic Granulite*	*Dry Eclogite*	*Dry Olivine*	*Wet Olivine*
f	1	1	1	0.1	1	1
$A_{ps}\,(Pa^{-n}s^{-1})$ [d]	8.57×10^{-28}	5.78×10^{-27}	3.17×10^{-21}	1.18×10^{-17}	1.43×10^{-16}	1.76×10^{-14}
n	4.0	4.7	3.2	3.5	4.0	3.0
$E\,(kJ\,mol^{-1})$	223	485	244	403	540	430
$V\,(m^3\,mol^{-1})$	0	0	0	2.72×10^{-5}	1.5×10^{-5}	1.0×10^{-5}
Thermal Parameters[e]						
$k\,(Wm^{-1}\,K^{-1})$	2.25	2.25		2.25	2.25	2.25
$C_p\,(Jkg^{-1}\,K^{-1})$	1250	1250		1250	1250	1250
$Q_p\,(W\,m^{-3})$	1.0×10^{-6}	0.4×10^{-6}		0.4×10^{-6}	0	0

[a] The density (ρ) is given by: $\rho=\rho_0[1-\alpha(T-T_0)]$, where α is the thermal expansion coefficient, T is the temperature (in $°C$) and T_0 is the surface temperature ($0\,°C$).
[b] The frictional-plastic yield stress (σ_y) is based on a Drucker Prager yield mechanism: $\sigma_y=Psin(\phi)+Ccos(\phi)$, where ϕ is the angle of internal friction, and C is the cohesion.
[c] Where stresses are below the plastic yield stress viscous deformation follows a dislocation creep power law, with an effective viscosity (η_{eff}) given by: $\eta_{eff}=\frac{1}{2}fA_{ps}^{\frac{-1}{n}}\dot{\varepsilon}_{II}'^{\frac{1-n}{2n}}e^{\frac{E+PV}{nRT_k}}$, where A_{ps} is the pre-exponential factor scaled to plane strain, n is the stress exponent, $\dot{\varepsilon}_{II}'$ is the second invariant of the deviatoric strain rate tensor, E is the activation energy, V is the activation volume, P is the pressure T_k is the absolute temperature, and R is the gas constant ($8.3145\,J\,mol^{-1}\,K^{-1}$).
[d] The experimental uniaxial strain viscosity pre-factor A_{uni} is scaled to plane strain A_{ps} using a scaling factor of $3^{\frac{n+1}{2}}2^{-1}$.
[e] k is the thermal conductivity, C_p is the specific heat capacity, and Q_p is the internal radiogenic heat production.

on the setup in Figure 2*a*. The upper crust, lower crust, mantle lithosphere and sub-lithospheric mantle have viscous rheologies of wet quartzite (Gleason & Tullis, 1995), dry Maryland diabase (Mackwell et al., 1998), dry olivine and wet olivine (Karato & Wu, 1993), respectively. Frictional-plastic deformation includes linear strain weakening, where all materials have a reduction in the friction angle and cohesion of 15° – 2° and 20 – 2 MPa, respectively, for cumulative plastic strain between 0.5 and 1.5. Other models (sets B, C, and D) examine variations in crustal density and/or lithosphere rheology, and also include the effect of lower crustal eclogitization. All the modifications in the models presented with respect to the reference model A, are listed in (Table 2).

The initial thermal structure is based on a conductive geotherm in the lithosphere, calculated using a surface heat flow of 54 $mW{\cdot}m^{-2}$, thermal conductivity of 2.25 $W{\cdot}m^{-1}{\cdot}K^{-1}$, and a radiogenic heat production in the upper and lower crust of 1 and 0.4 $W\mu{\cdot}m^{-3}$, respectively; there is no heat production in the mantle (Table 1). This geotherm has an initial Moho temperature of 650 °C and it intersects the mantle adiabat at the LAB (100 km depth) for the undisturbed lithosphere.

Below the LAB, the mantle is adiabatic, with a potential temperature of 1292 °C and adiabatic gradient of 0.4 $°C{\cdot}km^{-1}$. The initial geotherm is shown in Figure 2*c*. In the central region, the continental geotherm is linearly stretched following the gaussian-shaped thickening, such that the initial Moho temperature is constant everywhere. During the model run, the model boundaries have fixed temperature conditions using the initial temperature.

4 Eclogitization

Eclogitization is considered to affect the lower crust in areas of thickened crust and can result in a density increase that destabilizes the crustal root, leading to its detach-

Table 2. List of models with parameter modifications with respect to the reference values given in Table 1. The mantle lithosphere rheology is varied locally (in the central region) but remains as dry olivine at the sides for all models.

Model	**Eclogitization**	**Lower Crust Rheology**	**Local Mantle Lithosphere Rheology**	$\rho_{\mathbf{0}}^{*}$ [a] $(kg\,m^{-3})$	**Figure No.**
Reference					
A	✗	DMD[b]	DO[c]	2800	4
Set B					
B1	✓	DMD	DO	2800	5*a*
B2	✓	LMG[e]	DO	2800	5*b*
B3	✓	MG[d]	DO	2800	5*c*
Set C					
C1	✓	DMD	WO[f]	2800	6*a*
C2	✓	LMG	WO	2800	6*b*
C3	✓	MG	WO	2800	6*c*
Set D					
D1	✓	DMD	WO	2900	8*a*
D2	✓	LMG	WO	2900	8*b*
D3	✓	MG	WO	2900	8*c*

[a] $\rho_{\mathbf{0}}^{*}$ is the reference density in the upper crust in the perturbed region.
[b] DMD=Dry Maryland Diabase (Mackwell et al., 1998)
[c] DO=Dry Olivine (Karato & Wu, 1993)
[d] MG=Mafic Granulite (Y. F. Wang et al., 2012)
[e] LMG=Local Mafic Granulite (MG in the central region and DMD at the sides)
[f] WO=Wet Olivine (Karato & Wu, 1993)

ment (e.g., Leech, 2001). Metamorphic eclogitization can occur at temperatures and pressures greater than 600-800°C and 1.0-2.0 GPa, respectively, and the phase change is promoted by the presence of water (e.g., Ahrens & Schubert, 1975; Austrheim et al., 1997; Leech, 2001). In addition, in continental arcs, eclogite facies rocks can form as dense residues after magmatic differentiation in the crustal root; these are sometimes called arclogites (e.g., Ducea, Chapman, Bowman, & Triantafyllou, 2021). Therefore, it is possible that either metamorphic or magmatic eclogitization affected the SNSM, as it is an area of earlier shortening and it originally formed as a continental magmatic arc (e.g., Cardona et al., 2010; Ramírez et al., 2020).

Model A does not include eclogitization. In model sets B, C, and D, eclogitization in the lower crust occurs when its temperature is above 680°C and its pressure is above 1.2 GPa. The eclogite has a density of 3550 $kg{\cdot}m^{-3}$, representing full eclogitization of a basaltic lower crust (Austrheim et al., 1997). The rheology of eclogitized lower crust is poorly constrained. Laboratory measurements using a dry synthetic eclogite suggest relatively high strengths (e.g., Zhang & Green, 2007).

On the other hand, eclogitization may be accompanied by rheological weakening, suggesting that eclogites could be weaker than their protoliths and that the overall strength of eclogites is conditioned by the extent and rate of the reaction, which is strongly dependent on the amount of water available to trigger the phase change or the mechanisms by which water enters the rock (e.g., Austrheim et al., 1997; Leech, 2001). In our models, we use the viscous rheology of eclogite of Zhang and Green (2007) with a scaling factor (f) of 0.1 which reduces its viscosity by a factor of 10, to represent rheological weakening relative to the initial diabase rheology due to the phase change (Figure 2*d*). Additional model tests show that variations in eclogite rheology produce changes in the timing of crustal root detachment/removal; weaker eclogite rheologies produce a faster root removal (and vice-versa). However, these variations do not affect the magnitudes and general behavior of surface expressions (Figures S1 and S2 in supplementary material).

5 Results

5.1 Reference Model (Model A)

The results of model A are shown in Figures 3 and 4 and in Animation 1 (supplementary material). In this model, the imposed perturbation of the lithosphere-asthenosphere boundary (LAB) causes the lower part of the mantle lithosphere to undergo dripping (Figure 3). As the instability at the center founders, the mantle lithosphere is entrained from the sides and pulled towards the center. This results in thinning of the mantle lithosphere by 18 km at the sides. The drip detaches at ∼40 Ma, removing the lower 30 km of the mantle lithosphere in the central region. The shallower lithosphere is cool and therefore is too viscous to be removed (e.g., Conrad & Molnar, 1999). The crustal root is too buoyant to be removed but the drip causes a downward pull of the Moho by <3 km as it founders.

The evolution of topography on top of the perturbation is characterized by a total subsidence of 0.12 km produced by the pull of the dripping mantle lithosphere (Figure 4*a*). The drip detachment at ∼40 Ma has a minimal effect on topography, and it is followed by minor topographic changes (<0.1 km) related to continued mantle convection. Throughout the model evolution there is a gradual decrease in the gravity anomaly of ∼20 mGal (Figure 4*b*). This is mostly attributed to progressive mantle lithosphere thinning at the sides of the drip as the cold, dense mantle lithosphere is replaced with hot, buoyant sub-lithospheric mantle. There may also be a minor contribution from the downward deflection of the Moho during the drip. As the drip detaches at 40 Ma, there is an abrupt gravity anomaly increase of 28 mGal produced by the fast foundering of the cold, dense mantle lithosphere. Its effect on the surface gravity anomaly decreases rapidly as the detached mantle lithosphere sinks into the deeper mantle. The surface heat flow in-

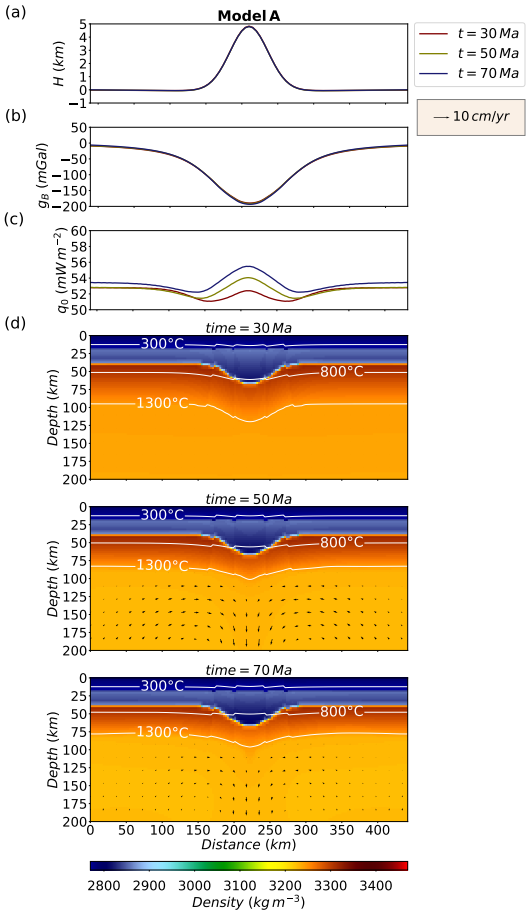

Figure 3. Evolution of the reference model (model A) at different times, showing the effect of the mantle lithosphere drip. (a) Surface Topography profiles (H). (b) Bouguer gravity anomaly profiles (g_B). (c) Surface heat flow profiles (q_0). (d) Snapshots of the density and thermal structure. Zero topography corresponds to the surface of the modeling domain.

creases from 50 to 58 mW·m^{-2} during the model evolution, due to internal radiogenic heating and conductive heating of the crust following lithosphere thinning (Figure 4*c*).

5.2 Effect of Lower Crustal Eclogitization (Model B1)

The results of model B1 are shown in Figures 4 and 5*a* and in Animation 2 (supplementary material). This model considers eclogitization of the deep crust; all other parameters are the same as in model A. The mantle lithosphere perturbation grows, drips, and detaches in a similar manner to model A (Figure 5*a*). However, the phase of instability growth prior to detachment is accompanied by progressive eclogitization of the lowermost crust. The deep crust is not initially in the eclogite stability field. Rather the phase change conditions are induced by the pull of the foundering mantle lithosphere and the temperature increase during lithosphere removal. The negative buoyancy of both the eclogite and mantle lithosphere perturbation results in detachment of the mantle lithosphere drip at 38 Ma, which is 2 Ma earlier than in model A. Eclogitization continues after drip detachment, and the crustal root starts to founder at ∼55 Ma because of its higher density. From 55 to 71 Ma, both the crustal root and underlying mantle lithosphere drip into the deeper mantle. The eclogitized crustal root detaches in two pulses (Animation

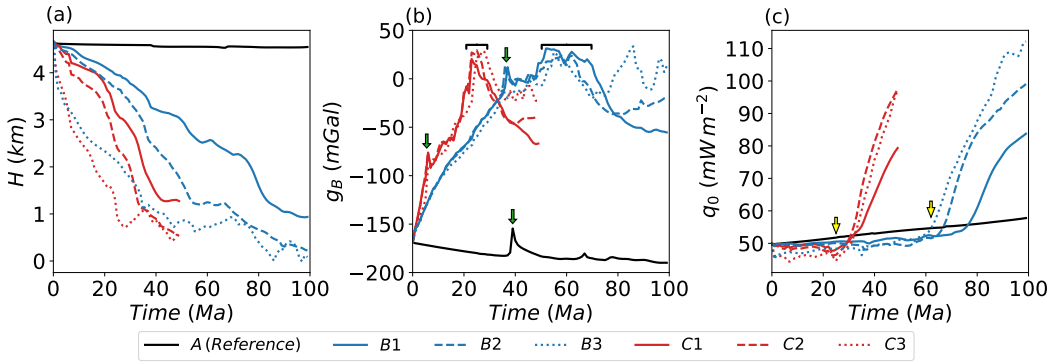

Figure 4. Time variation of surface observables averaged over a 50 km width centered over the initial perturbation, for the reference model (black) and model sets B (blue) and C (red). (a) Surface topography (H). (b) Bouguer gravity anomaly (g_B). Green arrows indicate the gravity response to the mantle lithosphere drip and black brackets indicate the response produced by crustal root removal. (c) Surface heat flow (q_0). Surface heat flow increases after the removal episode (indicated by yellow arrows) as the heat transfers through the crust by conduction.

2). At 59 Ma there is detachment of the lowermost root, which sinks together with the underlying mantle lithosphere. This leaves a ∼4 km thick eclogite layer that fully detaches from the non-eclogitized crust at 71 Ma and sinks to the deep mantle. Hereafter we refer to the time of root removal as the time when the eclogitized crustal root detaches and is no longer in contact with the non-eclogitized crust. Root removal leaves a thin crust (38 km) in the perturbed region, underlain by the upwelling sublithospheric mantle.

The evolution of topography in the perturbed region is influenced by the combined effects of the mantle lithosphere drip, eclogitization, and removal of the crustal root. From 0 to 71 Ma, the negative buoyancy of the growing mantle lithosphere instability, and the progressive eclogitization and foundering of the lower crust produce ∼2.4 km of surface subsidence (Figure 4*a*). Subsidence is not steady, but includes a period of higher subsidence rate (0.2 mm·yr^{-1}) at ∼36 Ma preceding detachment of the mantle lithosphere drip. This is followed by relaxation of the downward pull that results in a subsidence rate of 0.04 mm·yr^{-1} by 38 Ma. The pulses of crustal root detachment at 59 and 71 Ma are also associated with temporary decreases in subsidence lasting 3 and 1 Ma, respectively. This is explained by the upwelling of hot and buoyant sublithospheric mantle as the crustal root founders, which allows for temporary support of elevated topographies of 2.5 and 2.2 km at 59 and 71 Ma, respectively. After root removal, subsidence continues as the model comes into isostatic equilibrium with the new lithosphere structure, reaching an elevation of ∼1 km at 100 Ma.

Initially, the central region has a Bouguer gravity anomaly of -169 mGal due to the non-eclogitized crustal root (Figure 4*b*). As the crustal root undergoes eclogitization, the gravity anomaly increases and has a positive value between 47 to 72 Ma. As in model A, the mantle lithosphere drip produces a rapid peak of 12 mGal at 38 Ma. At the onset of crustal root dripping, there is an increase in the Bouger gravity anomaly, reaching a maximum of +30 mGal at ∼55 Ma. Detachment of the crustal root between 59 and 71 Ma causes small fluctuations in the gravity anomaly between 4 and 16 mGal. After root detachment, the gravity anomaly decreases and becomes negative as the eclogitized root sinks and is replaced by the buoyant sublithospheric mantle. The absence of

high-density mantle lithosphere in the central region and the decrease in crustal density due to localized heating result in a final Bouguer gravity anomaly of -56 mGal.

Between 0 and 70 Ma, the surface heat flow in the perturbed region is similar to that in model A (Figure 4*c*). The only difference is that the topographic changes and shallow deformation produced by crustal root removal generate a local decrease of <5 $mW{\cdot}m^{-2}$ (Figure 4*c*). From 70 to 100 Ma, model B1 exhibits a progressive increase in surface heat flow (up to 84.3 $mW{\cdot}m^{-2}$). This is caused by upwelling of the hot sublithospheric mantle and conductive heating of the overlying crust following root removal at 71 Ma. The largest increase in heat flow occurs after ∼79 Ma because the crust must be heated conductively from below.

This model shows that a positive gravity anomaly and a topographic high are simultaneously produced during crustal root removal between 46 and 72 Ma (Figure 4*a*). This trend is observed in the models discussed below, but the timescales and magnitudes vary with different rheologies and/or density parameters.

5.3 Lower Crustal Rheology (Set B)

Lithospheric rheology strongly affects drip dynamics (e.g., Göğüş & Pysklywec, 2008; H. Wang & Currie, 2017). In model set B, we test different lower crustal rheologies (Figure 2*d*; Table 2). The lower crust in model B1 has the rheology of dry Maryland diabase, as in reference model A. Model B2 uses the lower crustal rheology of mafic granulite (Y. F. Wang et al., 2012) in the thickened region and has dry Maryland diabase at the sides. We refer to this as local mafic granulite, assuming it represents a locally weaker composition associated with the previous magmatic arc. In model B3, the rheology of the whole lower crust is mafic granulite, producing a weak lower crust along the full profile.

The general dynamics of the three models are similar, with an initial mantle lithosphere drip, followed by removal of the eclogitied lower crust (Figure 5). Compared to model B1, the weaker lower crust allows for a slight increase in the removal rate, where detachment occurs at 64 Ma and 60 Ma for models B2 and B3, respectively, which are 7 Ma and 11 Ma earlier than in model B1. In models B2 and B3, elevations are consistently lower than in model B1, suggesting less lateral support for the topography owing to the weaker crust (Figure 4*a*).

There are also differences between the models after crustal root detachment. In model B2 after 80 Ma, there is crustal thinning of up to 6 km induced by the upwelling of the sublithospheric mantle because of the locally weak lower crustal rheology. The crustal thinning results in a higher Bouguer gravity anomaly, resulting in a final value of -25 mGal at 100 Ma (about 25 mGal higher than in model B1; Figure 4*b*). In addition, the final surface heat flow in model B2 is 15 $mW{\cdot}m^{-2}$ higher than in model B1 (Figure 4*c*). This is attributed to the combined effects of the thinner crust and the longer heating time due to earlier root detachment in model B2.

In model B3, crustal root removal and localized ascent of sublithospheric mantle in the perturbed region triggers lithosphere delamination in a similar fashion to the models of Krystopowicz and Currie (2013) (Figure S3). This occurs because the weak mafic granulite rheology allows for decoupling along the interface between the lower crust and mantle lithosphere. As the mantle lithosphere detaches laterally and sinks, a wide area of thinned lithosphere is produced, where the crust is thinned by ∼6 km and there is sublithospheric mantle upwelling. Consequently, Model B3 exhibits an uplift pulse of ∼0.3 km after lithosphere removal in the perturbed region, fluctuations in the gravity anomaly of up to 50 mGal and surface heat flow that is ∼30 $mW{\cdot}m^{-2}$ higher than in model B2.

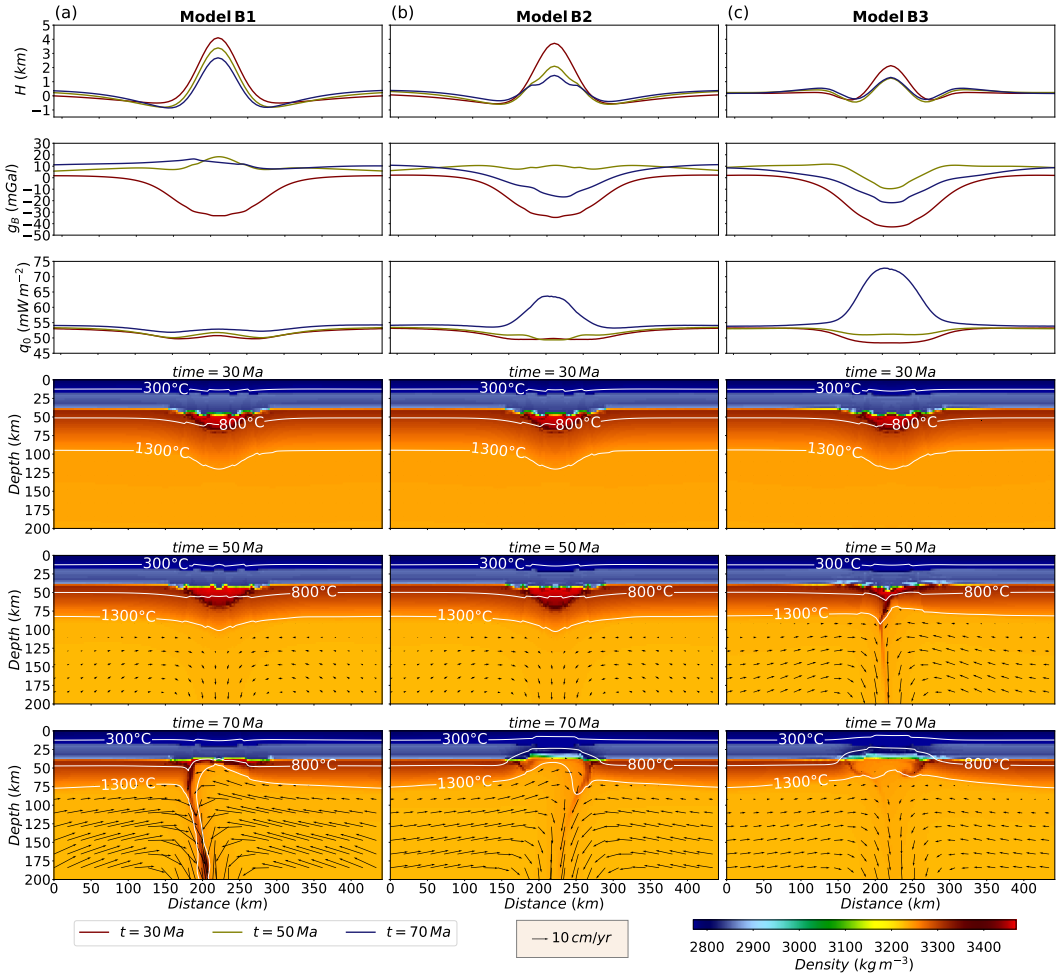

Figure 5. Evolution of (a) model B1, (b) model B2 and (c) model B3, including profiles of surface topography (H), Bouguer gravity anomaly (g_B) and surface heat flow (q_0), and snapshots of the density and thermal structure, at times before, during and after the main lithosphere removal episode. Model set B includes eclogitization and explores the effect of different lower crustal rheologies.

5.4 Mantle Lithosphere Rheology (set C)

Model set C tests the effect of mantle lithosphere rheology on drip dynamics. Model A and model set B use a dry olivine rheology for the mantle lithosphere. In set C, the mantle lithosphere in the perturbed region has the rheology of wet olivine. This is a simple approach to test a weaker mantle lithosphere (e.g., due to arc-related processes such as hydration and presence of melt). Models C1, C2 and C3 include lower crustal eclogitization and use the same modifications in the lower crust as models B1, B2 and B3, respectively (Table 2).

The results of model set C are shown in Figures 4 and 6. Model C1 is shown in Animation 3 as a representative model for the set. As in model set B, lithosphere removal is induced by both the mantle lithosphere perturbation and formation of dense eclogite. In model set C, the presence of the weaker mantle lithosphere speeds up the removal process. Root detachment occurs at 25, 26 and 28 Ma for C1, C2, and C3 respectively, 35-42 Ma earlier than in the comparable set B models. In set B, the mantle lithosphere

has a dry and strong rheology, which results in a slower drip, and thus the 30 km of crustal root can fully turn into eclogite before its detachment because the mantle lithosphere inhibits its descent. Conversely, in set C the mantle lithosphere drips at ∼8 Ma and eclogite starts dripping at ∼17 Ma because at that time there is no mantle lithosphere below. In set C, detachment of the eclogitized crustal root takes place in two pulses, as in set B, but the pulses occur within 5 Ma of each other, whereas they were ∼12 Ma apart in set B.

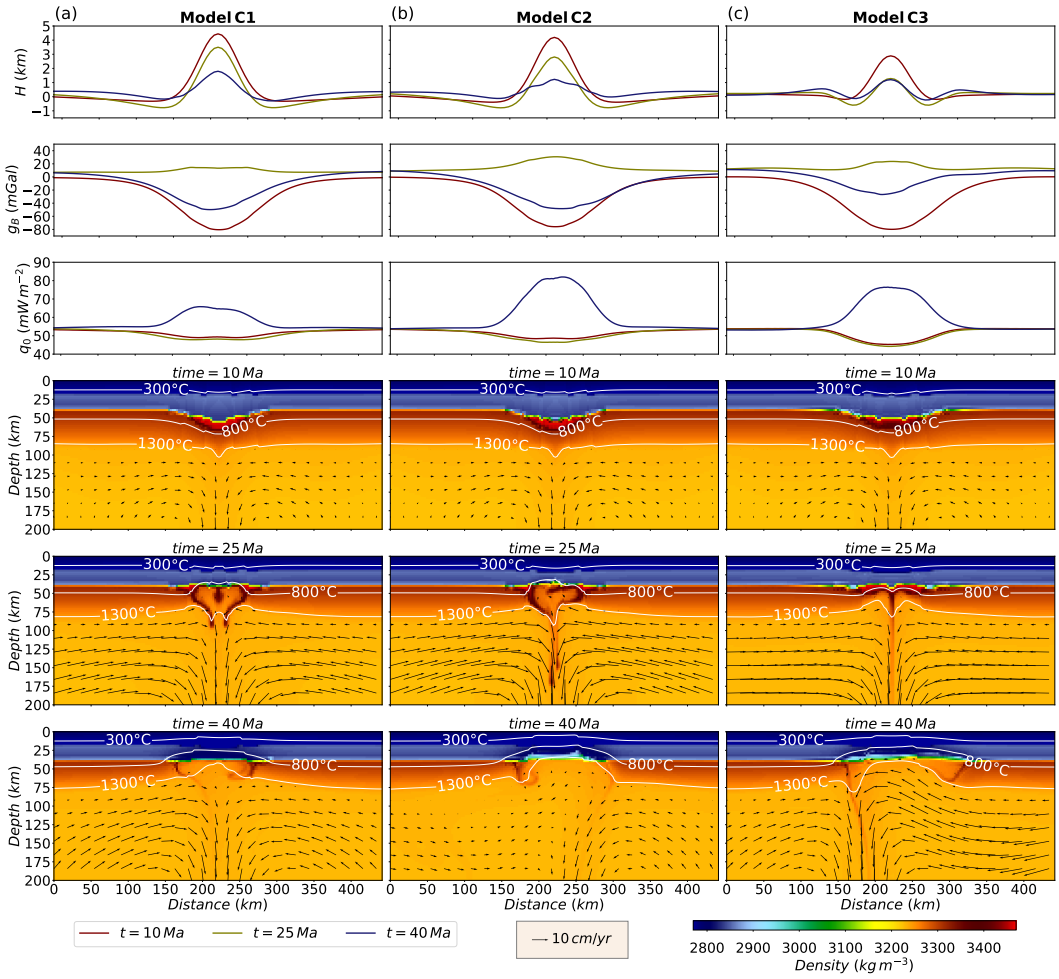

Figure 6. Evolution of (a) model C1, (b) model C2 and (c) model C3, including profiles of surface topography (H), Bouguer gravity anomaly (g_B) and surface heat flow (q_0), and snapshots of the density and thermal structure and at times before, during and after the main lithosphere removal episode. Model set C has a weaker mantle lithosphere rheology below the perturbed region. Models include eclogitization and explore the effect of different lower crustal rheologies.

The evolution of topography, Bouguer gravity anomaly, and surface heat flow (Figure 4) in sets B and C exhibit similar magnitudes and trends, but the timing is significantly different. For set C, the subsidence associated with the removal process, the increase in the Bouguer gravity anomaly produced by eclogitization and root removal, and the increase in surface heat flow produced by lithosphere thinning and subsequent conductive heating, all accur 30-40 Ma earlier than in set B. Because crustal root detachment occurs faster, it produces only one main peak in the gravity anomaly at ∼25 Ma,

and a positive gravity anomaly occurs for only ~5 Ma (between 23 and 28 Ma). Note that the results for set C are only shown to 50 Ma, as the crustal root is removed by 35 Ma in these models.

Models with a weak lower crust (C2 and C3) exhibit ~6 km crustal thinning following the removal event. As in model B2, in model C2 thinning is localized and is induced by the dripping of the crustal root and the sublithospheric mantle upwelling. As in model B3, in model C3 root removal induces regional delamination of the mantle lithosphere and thinning extends over a larger area.

5.5 Comparison of Surface Observables

The effect of lithosphere rheology on surface observables is summarized in Figure 7. This figure compares the surface elevation (Figure 7*a*), Bouguer gravity anomaly (Figure 7*b*), and surface heat flow (Figure 7*c*) in the central part of the model at the time of the maximum gravity anomaly ($t = t(g_{B\,max})$), and at 10 Ma after this ($t = t(g_{B\,max})$+ 10 Ma). The time of the maximum gravity anomaly corresponds to the time at which most of the crustal root has been removed through dripping; for most models this is 1-3 Ma before the time of full detachment. This allows for a comparison of the models at similar stages, and therefore an assessment of how removal of the deep lithosphere affects the surface observations.

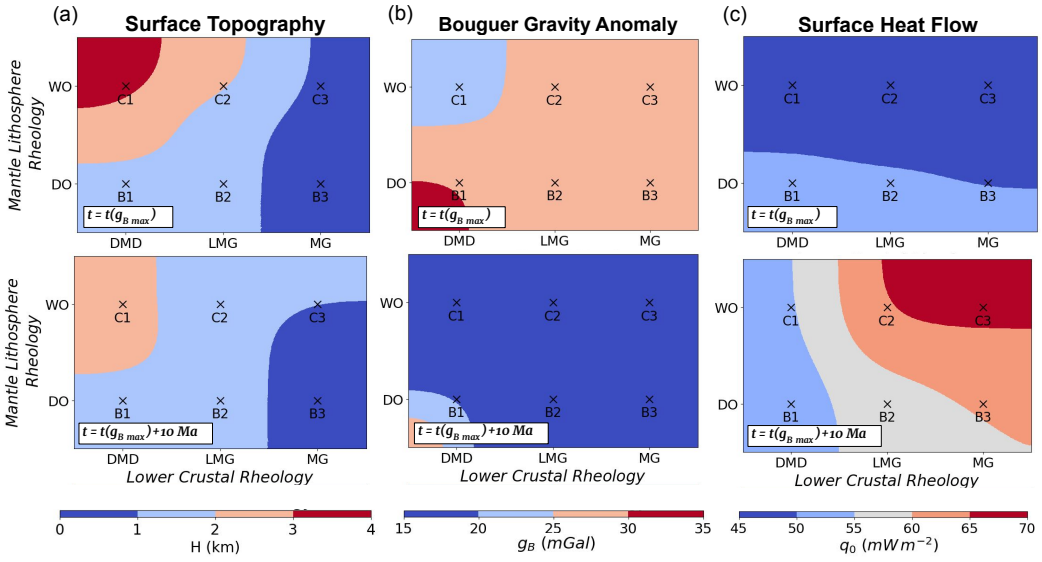

Figure 7. Magnitude of (a) surface topography (H), (b) Bouguer gravity anomaly (g_B), and (c) surface heat flow (q_0), averaged over a 50 km width centred on the perturbed region, at the time of the maximum gravity anomaly after crustal root removal (top) ($t = t(g_{B\,max})$), and 10 Ma after the peak gravity anomaly (bottom) ($t = t(g_{B\,max}) + 10\,Ma$). The plots show the results of model sets B and C as a function of mantle lithosphere rheology (y-axis) and lower crustal rheology (x-axis): DMD=Dry Maryland diabase; LMG=Local mafic granulite; MG=Mafic granulite; WO=Wet olivine; DO=Dry olivine.

The maximum gravity anomaly for all models is 20-30 mGal at $t(g_{B\,max})$, suggesting that there is not a significant difference between the models. However, a weaker mantle lithosphere rheology results in elevations that are 1-2 km higher than those for a stronger

mantle lithosphere. This is because if the removal of the crustal root is faster, $t(g_{B\,max})$ occurs sooner, there is less subsidence prior to $t(g_{B\,max})$ and the elevation at $t(g_{B\,max})$ is higher. Additionally, a weaker lower crustal rheology allows a faster subsidence rate resulting in lower elevations (within 1-2 km) compared to elevations for strong lower-crustal rheologies (within 3-4 km) because there is less lateral support. At $t(g_{B\,max})$+10 Ma the trend in the surface observables is the same as at $t(g_{B\,max})$, but for all models the magnitudes of gravity anomaly and topography are ∼10 mGal and ∼1 km lower, respectively, due to continued lower crustal heating that decreases its density, and isostatic equilibration.

Surface heat flow at $t(g_{B\,max})$ and $t(g_{B\,max})$+10 Ma exhibits different trends. At $t(g_{B\,max})$ variations in lower crustal rheology do not affect the surface heat flow, but surface heat flow is ∼5 mW·m^{-2} lower for a weaker mantle lithosphere because the drip is faster and there is less time for crustal heating before crustal root removal. At $t(g_{B\,max})$+ 10 Ma, the crust has started to be conductively heated by the hot sublithospheric mantle. Surface heat flow is higher (up to 60-70 mW·m^{-2}) for weaker lower crust and mantle lithosphere rheologies because the weak rheologies allow for more rapid removal, meaning that there is more time for the crust to be heated by conduction.

Our models show that eclogitization of the crustal root can create a local area of lithosphere thinning. This produces an increase in the gravity anomaly while mantle upwelling and lateral strength provide support for the load of the initial topography. Models in sets B and C show that eclogitization and crustal root removal produce a positive Bouguer gravity anomaly (0 to 30 mGal) together with an elevated topography (0 to 4 km). In all the models the magnitude of the Bouguer gravity anomaly at $t(g_{B\,max})$ is significantly lower than the observed anomaly in the SNSM (>+130 mGal) suggesting that additional factors are required to explain the excess of mass.

We note that in the models presented above, the initial crustal thickness in the central mountain region prior to lithosphere removal is fairly arbitrary as there are only limited observational constraints. Additional tests using different initial crustal thicknesses in the mountain region show that greater thicknesses produce faster lithosphere removal, higher subsidence rates, and more negative final gravity anomalies (see supplementary material).

5.6 Density of the SNSM Massif (Set D)

Gravity studies of northern Colombia argue that the crystalline basement rocks that underlie most of the SNSM massif appear to have a density that is higher than the surrounding rocks, owing to a more mafic composition (Ceron-Abril, 2008; Sanchez-Rojas & Palma, 2014; Sanchez & Mann, 2015). Sanchez and Mann (2015) suggest that the SNSM has a high density (comparable to lower crust densities). Consequently, we study the effects of a locally higher density in model set D, where the upper crust in the 125 km wide perturbed region has a density that is 100 kg·m^{-3} higher, consistent with the gravity studies. Models D1, D2, and D3 use the same parameter configurations as models C1, C2, and C3, respectively, differing only in the upper crust density in the central region (Table 2).

The results of model set D are shown in Figures 8 and 9, and Model D1 is shown in Animation 4. The temporal variations in surface observables are shown in Figures 9*a*–*c*, together with the results of model C1 as a reference. The overall behavior of the models in set D is similar to the equivalent models in set C. The presence of the dense upper crust has little effect on the timescales of root removal or on the surface heat flow. However, in set C the elevation is consistently lower (∼0.8 km lower), owing to the additional load of the dense rocks. The trend of the gravity anomaly is similar between sets C and D, but the presence of the high-density rocks results in systematically higher gravity anomalies in set D (∼+50 mGal).

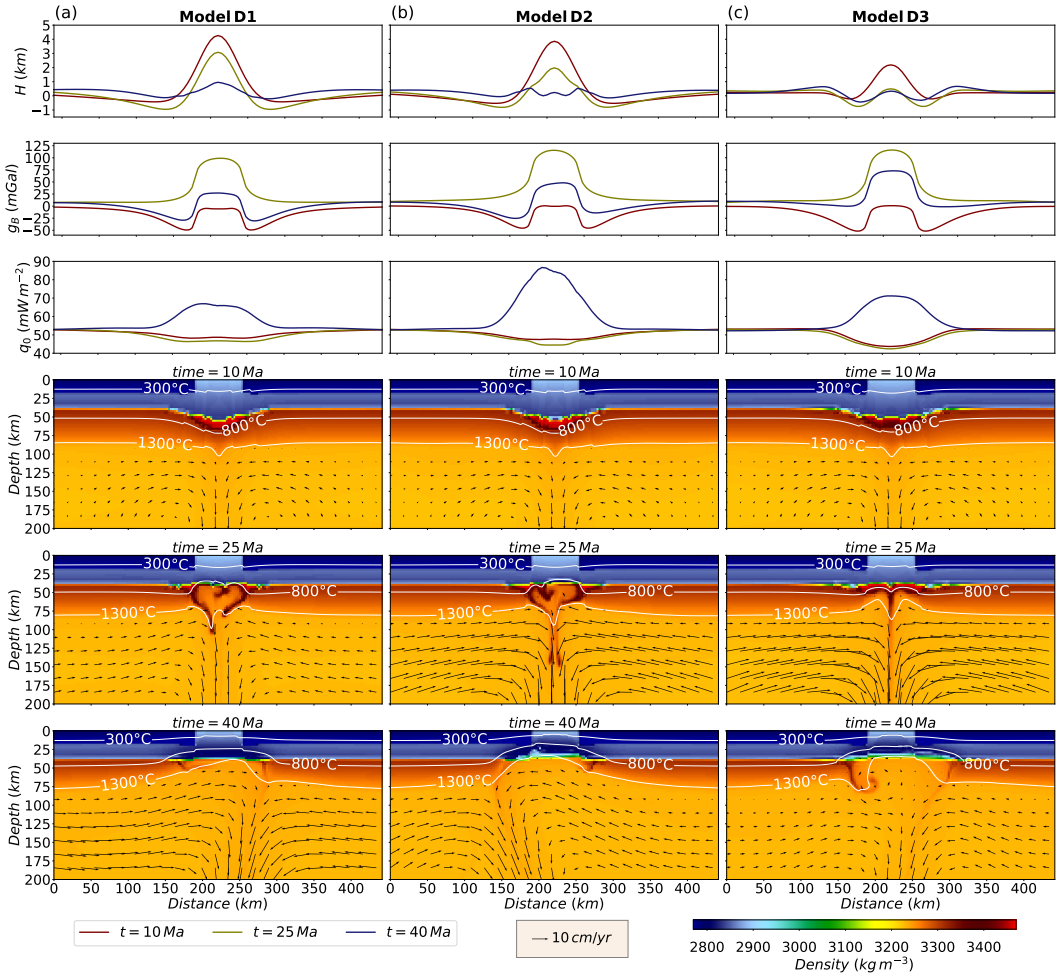

Figure 8. Evolution of (a) model D1, (b) model D2 and (c) model D3, including profiles of surface topography (H), Bouguer gravity anomaly (g_B) and surface heat flow (q_0), and snapshots of the thermal and density structure at times before, during and after the main lithosphere removal episode. Model set D is the same as set C, but it includes high-density upper crustal rocks in the perturbed region.

6 Geological and Geophysical Implications

6.1 Comparison With Observations

We select model D1 as our preferred model because the magnitudes of topography and Bouguer gravity anomaly are the closest to the SNSM observations. This is a consequence of the following points: (1) a weak local mantle lithosphere rheology (wet olivine) produces rapid removal (within 25 Ma) and allows less time for subsidence, (2) a strong lower-crustal rheology (dry Maryland diabase) provides more support for the load of the initial topography, and (3) the high-density upper crustal rocks in the perturbed region allow for a higher magnitude positive Bouguer gravity anomaly. This suggests that the gravitational effect of both the shallow high-density rocks of the exhumed basement and absence of a crustal root are required to account for the observed gravity anomaly. Figure 9*b* shows that the initial gravity anomaly of model D1 is negative (about -100 mGal) even with the presence of denser upper-crustal rocks, indicating that the effect of the crustal root dominates. After the lithosphere removal event, the Bouguer gravity becomes pos-

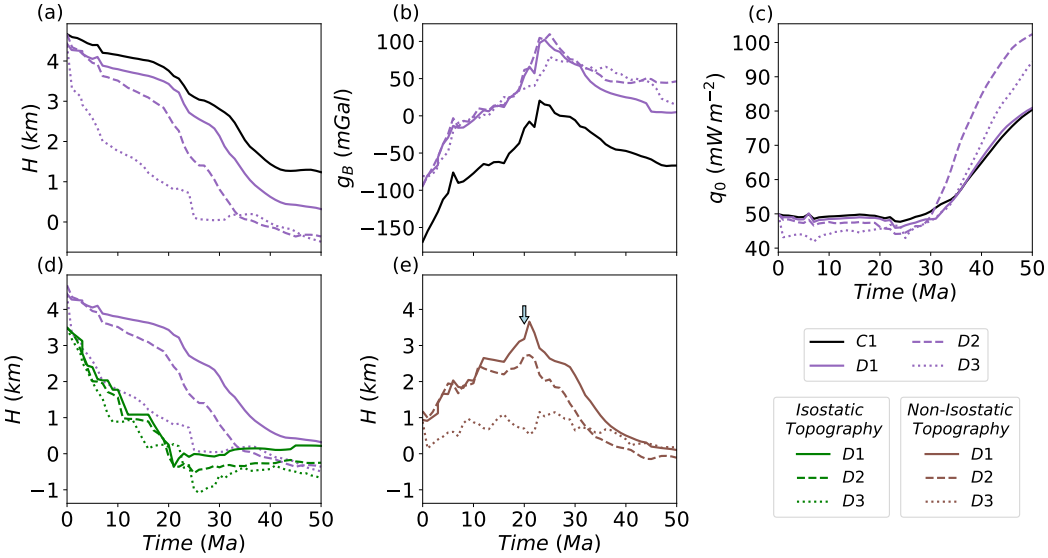

Figure 9. Time variation of surface observables, averaged over a 50 km width centered in the perturbed region for model set D, and model C1 as a reference. (a) Surface elevation (H) (total topography). (b) Bouguer gravity anomaly (g_B). (c) Surface heat flow (q_0). (d) Isostatic topography (green) with total topography for comparison (purple). (e) Non-isostatic topography. Blue arrow indicates time of maximum uplift rate (0.4 $mm\,yr^{-1}$) in model D1.

itive (about +100 mGal) and remains positive for almost 30 Ma while it progressively decreases.

Figure 10 compares the results of model D1 to the observations in the SNSM along the profile line $A{-}A'$ in Figure 1a at a model time of 23 Ma, corresponding to the maximum peak in the gravity anomaly, when the crustal root has been removed (∼2 Ma before full detachment). At this time the local Bouguer gravity anomaly is the result of the tradeoff between the absence of cool and dense mantle lithosphere underneath (lack of mass), the high-density shallow rocks in the SNSM (100 km·m^{-3} denser), and a locally thin crust (∼38 km) directly underlain by a shallow sublithospheric mantle (excess of mass near the Moho). While there are still uncertainties in the exact crustal thickness in the SNSM, this value is similar to the estimates of ∼35 km from Sanchez-Rojas and Palma (2014) and Poveda et al. (2018).

The observed Bouguer gravity anomaly and topography along $A{-}A'$ are from the EIGEN-GL04C Global gravity field model (Förste et al., 2008) and the ASTER Global Digital Elevation model V003 (Spacesystems & ASTER Science Team, 2019), respectively. The maximum modeled values for the Bouguer gravity anomaly and surface elevation are +103 mGal and 3.3 km, respectively, compared to the maximum observed values of +126 mGal and 5.1 km. The observed gravity shows that the positive peak is surrounded by two negative peaks that are associated with the low-density sediments of the lower Magdalena basin southwest of the SNSM and the Baja Guajira basin to the northeast. These gravity minima do not appear in the modeled gravity because the surrounding basins are not considered in the numerical model.

In the preferred model, surface heat flow immediately after removal is 46 mW·m^{-2}, and only reaches the values of 60-80 mW·m^{-2} reported by Quintero et al. (2019) for the SNSM after approximately 15 Ma. This implies that if lithosphere removal has occurred in the SNSM, both the gravity anomaly and surface topography must be sustained for

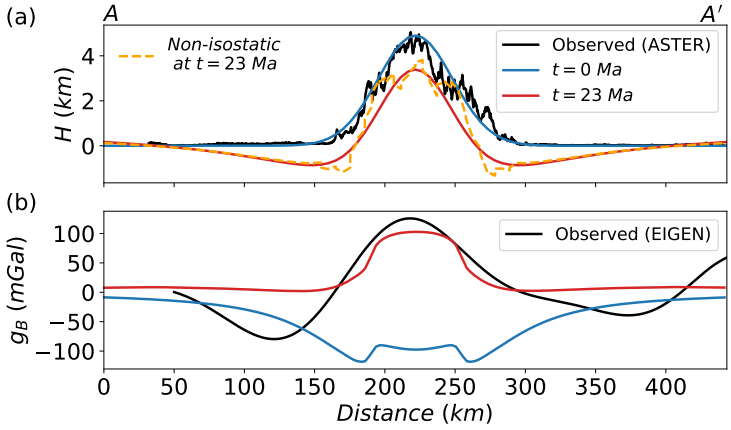

Figure 10. Comparison between topography and Bouguer gravity anomaly profiles of the preferred model (model D1) during root removal (∼2 Ma before full detachment at $t = 23$ Ma) with observed data. Initial topography (H) and gravity anomaly (g_B) profiles ($t = 0$ Ma) are shown for comparison (blue). (a) Modeled topography (red). Data from the ASTER global digital elevation model (black). Non-isostatic topography (orange). This shows that non-isostatic effects are localized in the elevated region. (b) Modeled Bouguer gravity anomaly (red). Data from the EIGEN-GL04C global gravity field model (black). Observed profiles are extracted along profile line $A - A'$ in Figure 1*a*.

at least 15 Ma to match the observations of heat flow. However, heat flow measurements in the study region are sparse and have large uncertainties, and additional data should be collected.

6.2 Isostatic vs. Non-Isostatic Topography

The models exhibit an overall subsidence in the central region as the result of the combined effects of the evolving density structure and mantle dynamics. To separate these effects, we calculate the isostatic topography, which is the topography that would be observed if there was isostatic equilibrium based on the density structure at each time (Figure 9*d*). Figure 9*e* shows the non-isostatic topography based on the difference between the total topography and isostatic topography. Non-isostatic effects involve the contribution to topography produced by both lateral lithosphere strength and vertical stresses from the dynamics of the deep lithosphere and underlying mantle. For models D1 and D2, the isostatic topography is significantly lower than the total topography throughout the removal episode, whereas model D3 is closer to isostatic balance throughout its evolution. This shows that the non-isostatic forces are more significant in models D1 and D2, compared to model D3. This is possibly due to the support provided by a rheologically stronger lower crust in model D1 (e.g., dry diabase), compared to the weaker crust in model D3 (e.g., mafic granulite). In model D2, the perturbed region has a mafic granulite lower crust, with dry diabase at the sides, and the role of non-isostatic forces is intermediate between models D1 and D3.

In model D1, the non-isostatic topography reaches a maximum of 3.5 km at 23 Ma (∼2 Ma before full detachment). Figure 10*a* shows that at 23 Ma the topography is predominantly non-isostatic. This suggests that the coexistence of a positive Bouguer gravity anomaly and high topography at this time is possible due to the delay in subsidence produced by non-isostatic effects.

6.3 Melting

Our study primarily considers the effect of lithosphere removal on surface topography, gravity and heat flow. The models also make additional predictions. As shown above, a lithosphere drip results in thinning of the lithosphere and causes upwelling of the sublithospheric mantle to fill the gap created by the drip. Decompression of upwelling mantle and simultaneous lower crustal heating may result in melting of both the mantle and crust, and therefore magmatism may accompany lithosphere removal (e.g., Kay & Mahlburg Kay, 1993; Mahlburg Kay et al., 1994). To assess this, we use the pressure-temperature conditions in model D1 to assess whether melting is predicted. Our calculations use the dry granite solidus from Elkins-Tanton (2005), and the solidus of partially hydrated peridotite with 0.15 wt% H2O (Katz et al., 2003), to consider lower crustal and mantle melting, respectively. The models do not include the transport of melt to the surface, nor the effects of melt on rheology and density.

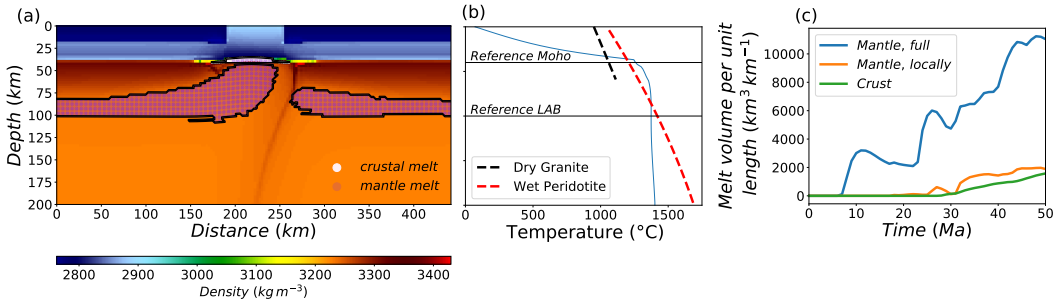

Figure 11. (a) Density structure of the preferred model (model D1) at $t = 33$ Ma (8 Ma after removal). Contours enclose regions where the P-T conditions are above the wet peridotite and dry granite solidi, for the mantle (purple infill) and lower crust (white infill), respectively. (b) Temperature profile at x=230 km and $t = 33$ Ma, with the dry granite (Elkins-Tanton, 2005) and the wet peridotite solidus (Katz et al., 2003). (c) Calculations of melt volume per unit length along strike for the lower crust. Local mantle melt volume is the melt volume in a 60 km width centered in the elevated region.

Figure 11$a - b$ shows model D1 at 10 Ma after root detachment ($t = 33$ Ma) to allow enough time for significant melt production. In the central region, melting of the sublithospheric mantle and deep crust are predicted. There is also a zone between 80 to 100 km depth outside of the main drip region where lower mantle lithosphere has been partially removed and conditions favor mantle melting.

Figure 11c shows the temporal evolution of mantle melt volume (per unit along strike) for both the full model domain and for a local 60 km wide region centered in the elevated zone. This is calculated by monitoring the regions of the model that are above the solidus, assuming a melt fraction per Kelvin above the solidus of 0.3% for the mantle (Katz et al., 2003) and 0.75% for the crust (Annen & Sparks, 2002). The onset of melting in the central region occurs at about 23 Ma, corresponding to mantle upwelling after root detachment and crustal heating. These calculations suggest that mantle and crustal melt volumes in the central region could be significant, with approximately equal amounts of each. The model also predicts that melts may be generated in the side regions, due to lithosphere thinning induced by lithosphere foundering in the central region.

6.4 Seismic Velocity Structure

In addition to melts, our models can be used to assess how lithosphere removal may affect the mantle seismic structure. For this, we use the temperature, pressure, and composition of model D1 to calculate the expected seismic P- and S-wave velocity structure. This uses Perple_X (Connolly, 2005) to obtain the bulk and shear moduli, assuming a pyrolite composition, with a correction for attenuation (van Wijk et al., 2008; Quiroga, 2022). The crust is excluded from this analysis, owing to uncertainties in crustal composition.

The calculated P- and S-wave velocities and their corresponding anomalies are shown in Figure 12 at a time of 23 Ma (time of the maximum Bouguer gravity anomaly during root removal). After removal of the dense crustal root, the gap created in the mantle lithosphere has a clear low velocity anomaly of up to -9.7 % in P-waves and -19.1 % in S-waves, with absolute values of 6.9 and 3.5 km·s^{-1}, respectively. The anomaly corresponds to the percentage difference compared to the average velocity at each depth. Note that the calculations do not include the effects of melt. Figure 12*a* shows where melt is predicted and therefore the seismic wave velocities could be even lower. These calculations indicate that lithosphere removal may be associated with a significant low-velocity anomaly. This could persist for >10 Ma following the removal event, as the lithosphere gap remains hot (Figure 12*c*).

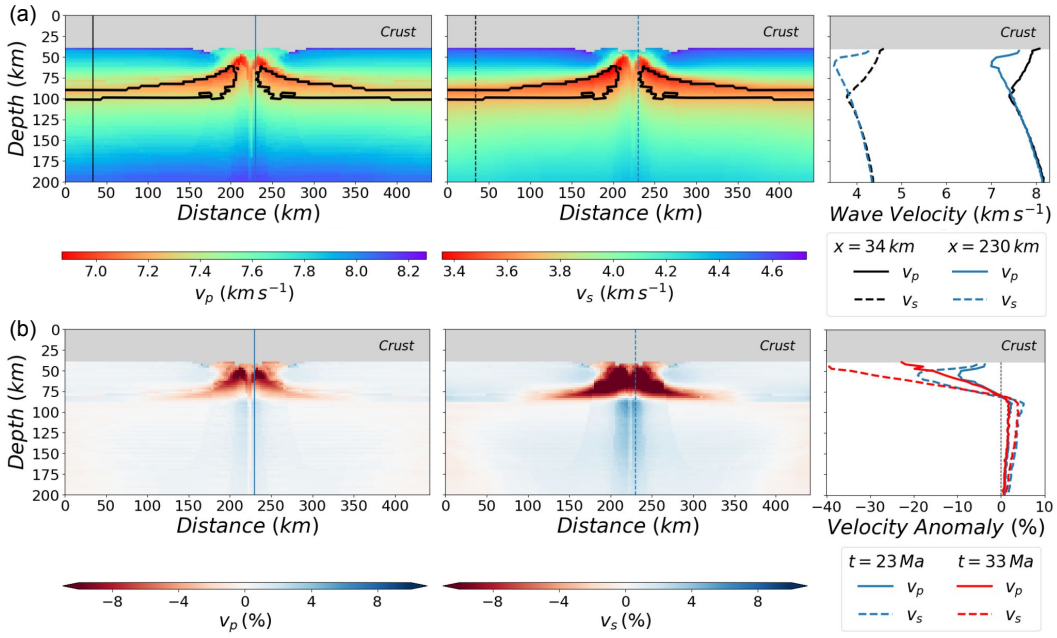

Figure 12. (a) Calculated seismic structure from model D1 at t = 23 Ma, showing P-wave velocities (left), S-wave velocities (center), and vertical profiles at the side (x = 34 km) and center (x = 230 km). Black contours enclose regions where the pressure and temperature conditions are above the peridotite solidus, which could have lower velocities. (b) P and S wave velocity anomalies and profiles at the side and center.

7 Discussion

7.1 Origin of the High Gravity Anomaly in the SNSM

The models presented above demonstrate that gravitational removal of an eclogitized crustal root can produce both a positive Bouguer gravity anomaly and an elevated topography. In model D1, this results in a gravity anomaly and topography of +103 mGal and 3.3 km, suggesting that a lithosphere drip is a viable mechanism to explain the SNSM observations. Based on the model results and geological observations, we suggest that a drip could have occurred at two possible times: in the Eocene (50-40 Ma) or within the last 2 Ma. These possibilities are discussed separately below. However, it is also possible that there was lithosphere removal at both times.

7.1.1 Lithosphere removal in the Eocene (50-40 Ma)

The first possibility is that lithosphere removal occurred in the Eocene. At this time, the SNSM was located in a volcanic arc region with subduction of the Caribbean plate below South America. In principle, there are not enough constraints to determine a specific time for this lithosphere removal episode. However, a removal event at 50-40 Ma would predate the slab flattening that has been proposed to explain the cessation of Paleocene-Eocene magmatic activity (e.g., Taboada et al., 2000), and therefore this timing has the advantage that a low-angle Caribbean slab would not block lithospheric foundering.

We suggest that removal at this time could have been driven by metamorphic eclogitization of thickened SNSM crust. Alternatively, root densification could have been produced by magmatic processes. Ducea, Chapman, Bowman, and Balica (2021) argue that melt extraction at an arc creates a lower layer of high-density "arclogite" rocks through magmatic differentiation. This process has been shown to promote gravitational removal even in garnet-free arcs where eclogite is not produced (e.g., Jull & Kelemen, 2001), which is possibly the case in the SNSM (e.g., Duque-Trujillo et al., 2019).

There were two main Paleocene-Eocene magmatic events that were separated by a magmatic gap. The first event produced the Paleocene leucogranites (age ∼65 Ma). e.g., Duque-Trujillo et al. (2019) argues that the protolith of this rocks had a mafic composition, under the stability field of amphibole, garnet, and rutile, which are all common minerals within arclogite assemblages (Ducea, Chapman, Bowman, & Triantafyllou, 2021). The second event created the Eocene Santa Marta Batholith (SMB) at 56 Ma. Duque-Trujillo et al. (2019) report that the SMB has substantial ultramafic garnet-free cumulates. Some of these have been classified as pegmatitic pyroxenites, perhaps showing evidence of a densified lower crust outside the garnet stability field, which could be gravitationally unstable. Duque-Trujillo et al. (2019) suggest that the SMB magmatism does not correspond to typical Andean-type subduction magmatism because it was localized, low-volume and short term (∼10 Ma). Instead, they propose that the melting of thickened lower crust could produce the required parental magma. A removal event at this time may explain the trends in magmatism. In our models crustal root removal takes place on timescales of ∼10 Ma following onset of root densification, and that lower-crustal and shallow sublithospheric mantle melts can be generated by decompression and heating after removal (Figure 11). This provides a mechanism to explain the anomalous Paleocene-Eocene magmatism. Continued heating can also explain the observations of high surface heat flow today (Quintero et al., 2019).

However, one problem with an Eocene removal event is that the surface expressions must persist for >40 Ma in order to explain the present-day high elevation and positive Bouguer gravity anomaly for the SNSM. Because the models in this study show only a short-lived period (∼5 Ma) of simultaneous high elevation and positive gravity anomaly, this may require additional factors such as elastic stresses, mantle upwelling, and support from the present-day Caribbean slab.

7.1.2 Recent lithosphere removal (<2 Ma)

The other possibility is that lithosphere removal occurred recently. Results from model D1 show that lithosphere removal produces a simultaneous positive Bouguer gravity anomaly and high topography similar to those observed in the SNSM. According to the models, the peak in the Bouguer gravity anomaly after lithosphere removal is short-lived (<5 Ma) suggesting that the current observations are compatible with recent removal. Additional evidence that favors a recent lithospheric drip comes from seismic observations. Seismic tomography studies consistently show low shear wave velocities (<3.8 $km{\cdot}s^{-1}$) in the SNSM region in the deep crust and shallow mantle (Syracuse et al., 2016; Poveda et al., 2018). These values are consistent with the shear wave velocities predicted for model D1 (Figure 12*a*).

The problem with a recent removal episode is that according to the models, the high Bouguer gravity anomaly and surface topography must be sustained for at least 15 Ma to allow enough heating time to match the observed surface heat flow values of 60-80 $mW{\cdot}m^{-2}$ (Quintero et al., 2019). Lithosphere removal within the last 2 Ma is predicted to have a lower surface heat flow (50-60 $mW{\cdot}m^{-2}$), although we note that there are uncertainties in both the observations and in the model thermal parameters . On the other hand, the elastic thickness in the SNSM is inferred to be 26-40 km (e.g., Arnaiz-Rodríguez & Audemard, 2014; Tassara et al., 2007), which suggests a cool lithosphere and relatively lower surface heat flow (<60 $mW{\cdot}m^{-2}$) (e.g., Hyndman et al., 2009). Another issue is that our calculations predict that lithosphere removal would induce lower crustal and upper mantle melting, whereas the last pulse of magmatism in the SNSM was at about 54-49 Ma (Duque-Trujillo et al., 2019). However, Figure 11*c* shows that the melt volume produced by lithosphere removal in the perturbed region is only significant >10 Ma after the removal episode. This means that if there was recent lithosphere removal there is possibly a low amount of melting in the mantle and deep lower crust that has not yet reached the surface.

7.2 Origin of High Topography in the SNSM

The models in this study show that a lithosphere removal episode produces subsidence rather than uplift. Upward forces from the upwelling sublithospheric mantle and lateral strength are only enough to delay subsidence providing some support. This is because our models start with a thick crust with initially high topography in the perturbed region and any non-isostatic forces have to overcome the load of the initial topography. However, the topographic variations in the models depend on the initial conditions, which are not well-known for the SNSM. For instance, lithosphere removal can induce uplift in models with an initially flat topography because the upward non-isostatic forces do not have to overcome the load of the initial topography (e.g., Göğüş & Pysklywec, 2008; H. Wang & Currie, 2017). Figure 9*e* shows that lithosphere removal in our models can create >3 km of non-isostatic topography meaning that non-isostatic effects can potentially produce uplift depending on the initial conditions. This may explain the observations of unexplained exhumation periods determined by Villagómez et al. (2011).

7.3 Additional Considerations

The models presented here investigate the dynamics of lithosphere removal and the associated surface expressions. One limitation is the 2D nature of the models. Previous studies show that 3D lithospheric drips occur faster and may produce greater topographic deflections, (e.g., Houseman & Gemmer, 2007; Pysklywec & Cruden, 2004). Also, Arnaiz-Rodríguez and Audemard (2014) suggest that elastic strength in the crust is important for supporting the SNSM massif. Kaus and Becker (2007) show that the inclusion of crustal elasticity in lithosphere drip models result in larger surface deflections and larger down-

welling rates. Future 3D models including elasticity are needed to assess the implications for the general dynamics and surface expressions of lithosphere removal.

Furthermore, the models address only the dynamics of the continental lithosphere and do not include the subducting Caribbean slab or regional tectonics. Seismic studies show that the SNSM region is underlain by the Caribbean slab, but there are uncertainties in the slab location and depth. It is unclear how the presence of the Caribbean plate may affect lithosphere removal, especially if the removal event occurred in the last 2 Ma. On one hand, the Caribbean plate may hinder the foundering of a crustal root; on the other hand, subduction may induce a lateral drag that promotes removal (e.g., Currie et al., 2015). Future models should include Caribbean plate subduction to assess its effect on the dynamics and structure of the overlying continent, including the SNSM.

8 Conclusions

This work uses numerical models of lithosphere removal to study the surface observations in the SNSM region of northwest Colombia. The models examine localized lithosphere removal below an area of pre-thickened crust and the associated variations in surface topography, Bouguer gravity, and surface heat flow. We find that foundering of a mantle lithosphere perturbation can induce eclogitization in the overlying crustal root, which is then gravitationally removed. This leaves a locally thinner crust ($\sim$38 km) underlain by the hot sublithospheric mantle, and results in a local excess of mass, a positive Bouguer gravity anomaly, and a progressive increase in surface heat flow as the crust heats through conduction. During removal, the formation of eclogite and the downward pull of the drip produce surface subsidence. During and after removal, the overall topography also depends on non-isostatic forces, such as lateral lithosphere strength and upwelling of the sublithospheric mantle. The timescales of removal and topographic changes depend on lithosphere rheology. Firstly, a local strong mantle lithosphere rheology (e.g., dry olivine) results in removal within 70 Ma, while a weak local rheology (e.g., wet olivine) results in removal within 25 Ma and allows less subsidence time than the stronger rheology. Also, a strong lower crustal rheology (e.g., dry diabase) provides more lateral support and sustains the initial topography for longer compared to a weak rheology (e.g., mafic granulite). We find that crustal eclogitization significantly modifies the drip dynamics. If it is not included (e.g., model A), the instability only involves the lowermost mantle lithosphere, there is no significant thinning of the lithosphere or changes in surface topography, and the Bouguer gravity anomaly remains negative (-150 to -200 mGal) due to the thick low-density crust. The gravity anomaly results confirm earlier studies that argue that the SNSM is not supported by an Airy-type crustal root (e.g., Case & Macdonald, 1973).

We propose that the high gravity anomaly and high topography in the SNSM region was produced by a lithosphere removal episode involving the eclogitization and removal of the crustal root. Our models show that the SNSM observations are compatible with a strong lower crust and a locally weak mantle lithosphere rheology (model D1), where crustal root removal produces a simultaneous positive Bouguer gravity anomaly (+103 mGal) and high topography (3.3 km), with a maximum non-isostatic topography of 3.5 km. In this case, the observed anomaly in the SNSM (>+100 mGal) requires both the high-density shallow crustal rocks (e.g., Sanchez & Mann, 2015) and gravitational lithosphere/crustal thinning. We suggest that lithosphere removal could have occurred either during the Paleocene-Eocene (40-50 Ma), possibly affecting regional magmatism, or very recently (in the last 2 Ma), creating an area of low seismic velocity in the shallow mantle. We prefer the interpretation of a more recent event because this can explain the observed low mantle seismic velocity, high topography and positive gravity anomaly. In either case, the models presented demonstrate that a gravitational removal event is a viable explanation for many of the uncommon observations in the SNSM.

9 Open Research

Our models use the Aspect code version 2.2.0 (Bangerth, Dannberg, Gassmoeller, & Heister, 2020). This software is open source and is availeable at: `https://github.com/geodynamics/aspect/tree/aspect-2.2`.

The parameter and input files developed for this study are also availeable at `https://github.com/d-quiroga/Lithosphere-removal-in-the-SNSM`. These correspond to models A and B1 as representative examples. The other models use the same inputs with the modifications expained in the text.

Acknowledgments

Research supported by an NSERC Discovery Grant to CAC. Models were run using resources provided by Compute Canada (www.computecanada.ca), now Digital Research Alliance of Canada. We thank the Computational Infrastructure for Geodynamics (geodynamics.org) which is funded by the National Science Foundation under awards EAR-0949446 and EAR-1550901 for supporting the development of ASPECT.

References

Ahrens, T. J., & Schubert, G. (1975). Gabbro-eclogite reaction rate and its geophysical significance. *Reviews of Geophysics*, *13*(2), 383–400. doi: 10.1029/RG013i002p00383

Annen, C., & Sparks, R. S. (2002). Effects of repetitive emplacement of basaltic intrusions on thermal evolution and melt generation in the crust. *Earth and Planetary Science Letters*, *203*(3-4), 937–955. doi: 10.1016/S0012-821X(02)00929-9

Arnaiz-Rodríguez, M. S., & Audemard, F. (2014). Variations in elastic thickness and flexure of the Maracaibo block. *Journal of South American Earth Sciences*, *56*, 251–264. doi: 10.1016/j.jsames.2014.09.014

Austrheim, H., Erambert, M., & Engvik, A. K. (1997). Processing of crust in the root of the Caledonian continental collision zone: The role of eclogitization. *Tectonophysics*, *273*(1-2), 129–153. doi: 10.1016/S0040-1951(96)00291-0

Bangerth, W., Dannberg, J., Gassmoeller, R., & Heister, T. (2020). *ASPECT v2.2.0.* Zenodo. Retrieved from `https://zenodo.org/record/3924604#.YA92S-hKiUk` doi: https://doi.org/10.5281/ZENODO.3924604

Bangerth, W., Dannberg, J., Gassmoeller, R., Heister, T., & Others. (2020). *ASPECT: Advanced Solver for Problems in Earth's ConvecTion, User Manual.* doi: https://doi.org/10.6084/m9.figshare.4865333

Bayona, G., Montes, C., Cardona, A., Jaramillo, C., Ojeda, G., Valencia, V., & Ayala-Calvo, C. (2011). Intraplate subsidence and basin filling adjacent to an oceanic arc–continent collision: A case from the southern caribbean-south america plate margin. *Basin Research*, *23*(4), 403–422.

Cardona, A., Valencia, V. A., Bayona, G., Duque, J., Ducea, M., Gehrels, G., ... Ruiz, J. (2010). Early-subduction-related orogeny in the northern Andes : Turonian to Eocene magmatic and provenance record in the Santa Marta Massif and Rancheria Basin , northern Colombia. *Terra Nova*, *23*(1), 26–34. doi: 10.1111/j.1365-3121.2010.00979.x

Case, I. E., & Macdonald, W. D. (1973). Regional gravity anomalies and crustal structure in Northern Colombia. *Bulletin of the Geological Society of America*, *84*(9), 2905–2916. doi: 10.1130/0016-7606(1973)84⟨2905:RGAACS⟩2.0.CO;2

Ceron-Abril, J. F. (2008). *Crustal structure of the Colombian Caribbean Basin and margins.* (PhD). University of South Carolina.

Connolly, J. A. (2005). Computation of phase equilibria by linear programming: A tool for geodynamic modeling and its application to subduction zone decarbonation. *Earth and Planetary Science Letters*, *236*(1-2), 524–541. doi: 10.1016/j.epsl.2005.04.033

Conrad, C., & Molnar, P. (1999). Convective instability of a boundary layer with temperature-and strain-rate-dependent viscosity in terms of 'available buoyancy'. *Geophysical Journal International*, *139*(1), 51–68.

Cornthwaite, J., Bezada, M. J., Miao, W., Schmitz, M., Prieto, G. A., Dionicio, V., ... Levander, A. (2021). Caribbean slab segmentation beneath northwest south america revealed by 3-d finite frequency teleseismic p-wave tomography. *Geochemistry, Geophysics, Geosystems*, *22*(4), e2020GC009431.

Currie, C. A., Ducea, M. N., DeCelles, P. G., Beaumont, C., Carrapa, B., & Kapp, P. (2015). Geodynamic models of cordilleran orogens: Gravitational instability of magmatic arc roots. *Geological Society of America Memoirs*, *212*, 1–22.

DeCelles, P. G., Carrapa, B., Horton, B., McNabb, J., Gehrels, G. E., Boyd, J., et al. (2015). The miocene arizaro basin, central andean hinterland: Response to partial lithosphere removal. *Geol. Soc. Am. Mem*, *212*, 359–386.

Ducea, M. N., Chapman, A. D., Bowman, E., & Balica, C. (2021). Arclogites and their role in continental evolution; part 2: Relationship to batholiths and volcanoes, density and foundering, remelting and long-term storage

in the mantle. *Earth-Science Reviews*, *214*(March 2021), 103476. doi: 10.1016/j.earscirev.2020.103476

Ducea, M. N., Chapman, A. D., Bowman, E., & Triantafyllou, A. (2021). Arclogites and their role in continental evolution; part 1: Background, locations, petrography, geochemistry, chronology and thermobarometry. *Earth-Science Reviews*, *214*(March 2021), 103375. doi: 10.1016/j.earscirev.2020.103375

Duque-Trujillo, J. F., Orozco-Esquivel, T., Sánchez, C. J., & Cárdenas-Rozo, A. L. (2019). Paleogene magmatism of the Maracaibo Block and its tectonic significance. In F. Cediel & R. Shaw (Eds.), *Frontiers in earth sciences* (pp. 551–601). Medellín: Springer, Cham. doi: 10.1007/978-3-319-76132-9_7

Elkins-Tanton, L. T. (2005). Continental magmatism caused by lithospheric delamination. *Special Paper of the Geological Society of America*, *388*(27), 449–461. doi: 10.1130/0-8137-2388-4.449

Förste, C., Schmidt, R., Stubenvoll, R., Flechtner, F., Meyer, U., König, R., ... others (2008). The geoforschungszentrum potsdam/groupe de recherche de geodesie spatiale satellite-only and combined gravity field models: Eigen-gl04s1 and eigen-gl04c. *Journal of Geodesy*, *82*(6), 331–346.

Freymueller, J. T., Kellogg, J. N., & Vega, V. (1993). Plate motions in the north Andean region. *Journal of Geophysical Research*, *98*(B12), 853–863. doi: 10.1029/93jb00520

Gleason, G. C., & Tullis, J. (1995). A flow law for dislocation creep of quartz aggregates determined with the molten salt cell. *Tectonophysics*, *247*(1-4), 1–23.

Göğüş, O. H., Pysklywec, R. N., Şengör, A., & Gün, E. (2017). Drip tectonics and the enigmatic uplift of the central anatolian plateau. *Nature communications*, *8*(1), 1–9.

Göğüş, O. H., & Pysklywec, R. N. (2008). Near-surface diagnostics of dripping or delaminating lithosphere. *Journal of Geophysical Research: Solid Earth*, *113*(11), 1–11. doi: 10.1029/2007JB005123

Hales, T. C., Abt, D. L., Humphreys, E., & Roering, J. J. (2005). A lithospheric instability origin for columbia river flood basalts and wallowa mountains uplift in northeast oregon. *Nature*, *438*(7069), 842–845.

Heister, T., Dannberg, J., Bangerth, W., & Gassm, R. (2017). High Accuracy Mantle Convection Simulation through Modern Numerical Methods . II : Realistic Models and Problems. *Geophysical Journal International*, *210*(2), 833–851. doi: https://doi.org/10.1093/gji/ggx195

Houseman, G. A., & Gemmer, L. (2007). Intra-orogenic extension driven by gravitational instability: Carpathian-pannonian orogeny. *Geology*, *35*(12), 1135–1138.

Houseman, G. A., Mckenzie, D. P., & Molnar, P. (1981). Convective instability of a thickened boundary layer and its relevance for the thermal evolution of continental convergent belts. *Journal of Geophysical Research*, *86*, 6115-6132.

Hyndman, R., Currie, C., Mazzotti, S., & Frederiksen, A. (2009). Temperature control of continental lithosphere elastic thickness, te vs vs. *Earth and Planetary Science Letters*, *277*(3-4), 539–548.

Jull, M., & Kelemen, P. B. (2001). On the conditions for lower crustal convective instability. *Journal of Geophysical Research: Solid Earth*, *106*(B4), 6423–6446. doi: 10.1029/2000jb900357

Karato, S.-i., & Wu, P. (1993). Rheology the upper mantle : Synthesis. *Science*, *260*(May), 771–778.

Katz, R. F., Spiegelman, M., & Langmuir, C. H. (2003). A new parameterization of hydrous mantle melting. *Geochemistry, Geophysics, Geosystems*, *4*(9), 1–19. doi: 10.1029/2002GC000433

Kaus, B. J., & Becker, T. W. (2007). Effects of elasticity on the rayleigh–taylor instability: implications for large-scale geodynamics. *Geophysical Journal International*, *168*(2), 843–862.

Kay, R., & Mahlburg Kay, S. (1993). Delamination and delamination magmatism.

Tectonophysics, *219*(1-3), 177–189. doi: 10.1016/0040-1951(93)90295-U

Kronbichler, M., Heister, T., & Bangerth, W. (2012). High accuracy mantle convection simulation through modern numerical methods. *Geophysical Journal International*, *191*(1), 12–29. doi: 10.1111/j.1365-246X.2012.05609.x

Krystopowicz, N. J., & Currie, C. A. (2013). Crustal eclogitization and lithosphere delamination in orogens. *Earth and Planetary Science Letters*, *361*, 195–207.

Leech, M. L. (2001). Arrested orogenic development: Eclogitization, delamination,and tectonic collapse. *Earth and Planetary Science Letters*, *185*(1-2), 149–159. doi: 10.1016/S0012-821X(00)00374-5

Londoño, J. M., Vallejo, K., & Quintero, S. (2020). Detailed seismic velocity structure of the Caribbean and Nazca Plates beneath Valle Medio del Magdalena region of NE Colombia. *Journal of South American Earth Sciences*, *103*(August 2019). doi: 10.1016/j.jsames.2020.102762

Mackwell, S. J., Zimmerman, M. E., & Kohlstedt, D. L. (1998). High-temperature deformation of dry diabase with application to tectonics on Venus. *Journal of Geophysical Research: Solid Earth*, *103*(1), 975–984. doi: 10.1029/97jb02671

Mahlburg Kay, S., Coira, B., & Viramonte, J. (1994). Young mafic back arc volcanic rocks as indicators of continental lithospheric delamination beneath the Argentine Puna plateau, central Andes. *Journal of Geophysical Research*, *99*(B12), 24323–24339.

Montes, C., Bayona, G., Jaramillo, C., Ojeda, C., Molina, M., & Herrera, F. (2005). Uplift of the Sierra Nevada de Santa Marta and subsidence in the Cesar-Rancheria valley : Rigid-beam pivot model. *Sixth International Symposium of Andean Geodynamics*(January), 520–523.

Peraza, W. L. (2014). *Precipitación media total anual. promedio multianual 1981 - 2010 [mapa].* Instituto de Hidrologia, Meteorologia y Estudios Ambientales - IDEAM.

Pindell, J., Kennan, L., Maresch, W. V., Stanek, K., Draper, G., & Higgs, R. (2005). Plate-kinematics and crustal dynamics of circum-caribbean arc-continent interactions: Tectonic controls on basin development in proto-caribbean margins. *Special Papers-Geological Society of America*, *394*, 7.

Poveda, E., Julià, J., Schimmel, M., & Perez-Garcia, N. (2018). Upper and Middle Crustal Velocity Structure of the Colombian Andes From Ambient Noise Tomography: Investigating Subduction-Related Magmatism in the Overriding Plate. *Journal of Geophysical Research: Solid Earth*, *123*(2), 1459–1485. doi: 10.1002/2017JB014688

Pysklywec, R. N., & Cruden, A. R. (2004). Coupled crust-mantle dynamics and intraplate tectonics: Two-dimensional numerical and three-dimensional analogue modeling. *Geochemistry, Geophysics, Geosystems*, *5*(10).

Quandt, D., Trumbull, R. B., Altenberger, U., Cardona, A., Romer, R. L., Bayona, G., ... Guzman, G. (2018). The geochemistry and geochronology of Early Jurassic igneous rocks from the Sierra Nevada de Santa Marta, NW Colombia, and tectono-magmatic implications. *Journal of South American Earth Sciences*, *86*(November 2017), 216–230. doi: 10.1016/j.jsames.2018.06.019

Quintero, W., Campos-Enriquez, O., & Hernandez, O. (2019). Curie point depth, thermal gradient, and heat flow in the Colombian Caribbean (northwestern South America). *Geothermal Energy*, *7*(1). doi: 10.1186/s40517-019-0132-9

Quiroga, D. E. (2022). *Numerical models of lithosphere removal in the sierra nevada de santa marta, colombia* (Unpublished master's thesis). University of Alberta.

Ramírez, D. A., Correa-Martínez, A. M., Zapata-Villada, J. P., & Rodríguez, G. (2020). Tectono-magmatic implications of the Jurassic volcanic and volcanoclastic record of the Santa Marta Massif (Colombia). *Journal of South American Earth Sciences*, *104*(September), 102866. doi: 10.1016/j.jsames.2020.102866

Rose, I., Buffett, B., & Heister, T. (2017). Stability and accuracy of free surface time integration in viscous flows. *Physics of the Earth and Planetary Interiors*, *262*, 90–100. doi: 10.1016/j.pepi.2016.11.007

Saleeby, J., Le Pourhiet, L., Saleeby, Z., & Gurnis, M. (2012). Epeirogenic transients related to mantle lithosphere removal in the southern Sierra Nevada region, California, part I: Implications of thermomechanical modeling. *Geosphere*, *8*(6), 1286–1309. doi: 10.1130/GES00746.1

Sanchez, J., & Mann, P. (2015). Integrated structural and basinal analysis of the Cesar–Rancheria Basin, Colombia: Implications for its tectonic history and petroleum systems. *AAPG Memoir*, *108*, 431–470. doi: 10.1306/13531945M1083648

Sanchez-Rojas, J., & Palma, M. (2014). Crustal density structure in northwestern south america derived from analysis and 3-d modeling of gravity and seismicity data. *Tectonophysics*, *634*, 97–115.

Spacesystems, & ASTER Science Team. (2019). *ASTER global digital elevation model v003 [data set].* (NASA EOSDIS Land Processes DAAC. Accessed 2021-01-07)

Spikings, R., Cochrane, R., Villagomez, D., Van der Lelij, R., Vallejo, C., Winkler, W., & Beate, B. (2015). The geological history of northwestern South America: From Pangaea to the early collision of the Caribbean Large Igneous Province (290-75 Ma). *Gondwana Research*, *27*(1), 95–139. doi: 10.1016/j.gr.2014.06.004

Syracuse, E. M., Maceira, M., Prieto, G. A., Zhang, H., & Ammon, C. J. (2016). Multiple plates subducting beneath Colombia, as illuminated by seismicity and velocity from the joint inversion of seismic and gravity data. *Earth and Planetary Science Letters*, *444*, 139–149. Retrieved from `http://dx.doi.org/10.1016/j.epsl.2016.03.050` doi: 10.1016/j.epsl.2016.03.050

Taboada, A., Rivera, L. A., Fuenzalida, A., Cisternas, A., Philip, H., Bijwaard, H., ... Rivera, C. (2000). Geodynamics of the northern Andes. *Tectonics*, *19*(5), 787–813.

Tassara, A., Swain, C., Hackney, R., & Kirby, J. (2007). Elastic thickness structure of South America estimated using wavelets and satellite-derived gravity data. *Earth and Planetary Science Letters*, *253*(1-2), 17–36. doi: 10.1016/j.epsl.2006.10.008

Telford, W. M., Geldart, L., & Sheriff, R. (1990). *Applied geophysics* (2nd ed., Vol. 69) (No. 1-2). Cambridge University press.

Tschanz, C. M., Marvin, R. F., Cruz, J. B., Menhnert, H. H., & Cebula, G. T. (1974). Geologic Evolution of the Sierra Nevada de Santa Marta, Northeastern Colombia. *Geological Society of America Bulletin*, *85*(2), 273–284. doi: https://doi.org/10.1130/0016-7606(1974)85⟨273:GEOTSN⟩2.0.CO;2

Van Der Hilst, R., & Mann, P. (1994). Tectonic implications of tomographic images of subducted lithosphere beneath northwestern South America. *Geology*, *22*(5), 451–454. doi: 10.1130/0091-7613(1994)022⟨0451:TIOTIO⟩2.3.CO;2

van Wijk, J., van Hunen, J., & Goes, S. (2008). Small-scale convection during continental rifting: Evidence from the Rio Grande rift. *Geology*, *36*(7), 575–578. doi: 10.1130/G24691A.1

Vargas, C. A. (2020). Subduction Geometries in Northwestern South America. In J. T. Gómez & A. O. Pinilla-Pachon (Eds.), *The geology of colombia* (Vol. 4, pp. 397–422). Bogotá: Servicio Geológico Colombiano, Publicaciones Geológicas Especiales 38. doi: https://doi.org/10.32685/pub.esp.38.2019.11

Vargas, C. A., Alfaro, C., Briceño, L. A., Alvarado, I., & Quintero, W. (2009). Mapa geotérmico de colombia - 2009 [Paper in Spanish] Geothermal Map of Colombia-2009. *Asociación Colombiana de Geólogos y Geofisicos del Petróleo (ACGGP)*(3), 1–5.

Villagómez, D., Spikings, R., Mora, A., Guzmán, G., Ojeda, G., Cortés, E., & Lelij,

R. V. D. (2011). Vertical tectonics at a continental crust - oceanic plateau plate boundary zone : Fission track thermochronology of the Sierra Nevada de Santa Marta , Colombia. *Tectonics*, *30*(4). doi: 10.1029/2010TC002835

Wang, H., & Currie, C. A. (2017). Crustal deformation induced by mantle dynamics: Insights from models of gravitational lithosphere removal. *Geophysical Journal International*, *210*(2), 1070–1091. doi: 10.1093/gji/ggx209

Wang, H., Currie, C. A., & DeCelles, P. G. (2015). Hinterland basin formation and gravitational instabilities in the central andes: Constraints from gravity data and geodynamic models. *Geol. Soc. Am. Mem*, *212*, 387–406.

Wang, Y. F., Zhang, J. F., Jin, Z. M., & Green, H. W. (2012). Mafic granulite rheology: Implications for a weak continental lower crust. *Earth and Planetary Science Letters*, *353-354*, 99–107. Retrieved from `http://dx.doi.org/10.1016/j.epsl.2012.08.004` doi: 10.1016/j.epsl.2012.08.004

Zhang, J., & Green, H. W. (2007). Experimental investigation of eclogite rheology and its fabrics at high temperature and pressure. *Journal of Metamorphic Geology*, *25*(2), 97–115. doi: 10.1111/j.1525-1314.2006.00684.x